Research Article

Superdirective Circular Arrays of Electric and Huygens Dipole Elements

Richard W. Ziolkowski[ID]

The University of Arizona, Tucson, AZ 85721, USA

Abstract — Uniform circular arrays (UCAs) provide both omnidirectional (360°) and directive (sector) coverage of the azimuthal plane. Superdirective versions with unidirectional, high front-to-back ratio (FTBR) properties could provide the radiated field characteristics being pursued for NextG wireless networks and their perceived applications. Typical UCA configurations – full, semi-circular, and sector – that radiate vertically-polarized (VP) fields and are composed of either omnidirectional electric dipole elements or unidirectional Huygens dipole elements are analyzed first with conventional methods as reference cases. These omni- and uni-directional element configurations are then treated with several optimization techniques: the classic Rayleigh-quotient (RQ) method and its unidirectional-constrained version; the eigenbeam decomposition and synthesis (EBDS) technique used to design superdirective acoustic receiving arrays; and the Bessel-azimuthal multipole (BEAM) approach developed herein. Several arrays are identified as being superdirective with extremely high FTBR values. The performance characteristics of the arrays of unidirectional elements are demonstrated to be superior in general. Moreover, it is shown that larger radius arrays with RQ-specified excitation amplitudes are robust to changes in them whereas the outcomes of the corresponding small radius versions are not. On the other hand, the BEAM-optimized densely-packed small-radius superdirective arrays are quite tolerant to those variations while generating unidirectional pseudo-needle beams.

Keywords — Directivity, Huygens dipole antennas, Multipoles, Needle radiation, Optimization, Superdirective arrays, Uniform circular arrays.

Citation — Richard W. Ziolkowski, "Superdirective circular arrays of electric and huygens dipole elements," *Electromagnetic Science*, vol. 2, no. 1, article no. 0050072, 2024. doi: 10.23919/emsci.2024.0007.

I. Introduction

Circular arrays have facilitated numerous acoustic and electromagnetic (EM) applications over several decades. They can readily provide omnidirectional coverage in both transmission (e.g., broadcasting – information dissemination) and reception (e.g., sensing – information capture) modalities. As phased-array systems, they are attractive for use in multifunction radar and communication applications that require beam steering over the entire azimuth plane. Moreover, they offer the ability to combine both their omni and directional properties in a single, simple system. They do not have left-right ambiguities, and their directive beams can be scanned with uniform behavior over the entire 360° azimuthal space.

Ring aerials (uniform circular arrays (UCAs) of dipole antennas) as omni and directional systems have seen nearly a century of development and applications, e.g., [1]–[3].

Their early applications included TV broadcasting, radio monitoring, and remote sensing (e.g., radars). More recently, UCAs have provided wireless communication coverage over the azimuthal plane, e.g., [4]–[6]. They have been applied as the basis for smart antennas (adaptive arrays) to facilitate mobile communications, e.g., [7], [8]. Very large resonant UCAs and their consequent extreme properties have been studied for many years, e.g., [9]–[12].

Electrically steerable parasitic array radiator (ESPAR) systems are notable UCA examples. Their original concept, a circular array of parasitic dipole (monopole) elements excited by a concentric, driven (active) dipole (monopole) element was considered by Harrington in the seminal paper [13]. The specific term appears to have originated in the article [14]. They have more recently been developed to achieve electronic beam forming/steering over the entire azimuthal plane [15]–[21]. They avoid the cost of massive, adaptive phased arrays in which each of their elements are active in

order to facilitate precise control of their amplitudes and phases. ESPAR systems can direct radiation to intended recipients and steer radiation nulls toward any interfering signals. The radiation nulls and main lobe gains complement each other to maximize the system SINR (signal-to-interference-noise ratio). As a consequence, the antenna's main lobe gain dramatically decreases the required transmission power for a set range. Moreover, directed radiation also helps alleviate health concerns that might accompany such radiators.

They have been adapted for direction-of-arrival (DOA) determination for position location services, e.g., [22]–[26], as well as for V2V (vehicle-to-vehicle) communications and remote sensing e.g., [27], [28]. These are particularly attractive features for NextG wireless systems. Metasurface versions of ESPARs that mimic their functionalities are being developed, e.g., [6], [29]–[33]. UCAs, ESPARs, and their pattern-reconfigurable advantages have been realized with standard radiating elements that are more complicated than dipoles, such as log-periodic, Vivaldi, and horn antennas, e.g., [26], and other more exotic elements, notably plasmas antennas, e.g., [34]–[42].

Because NextG systems require highly directive beams to minimize power requirements, provide low-probability-of-intercept (LPI) performance, and to overcome propagation losses particularly at millimeter-wave (mm-wave) frequencies, arrays with superdirective properties would be very advantageous. As will be discussed in further depth below, an array is said to be superdirective if its directivity exceeds the value obtained when the array is uniformly excited. The concept originated over a century ago with the seminal needle-radiation paper by Oseen [43]. There have been numerous articles that have examined the maximum directivity and, hence, gain (i.e., gain equals efficiency times directivity) in the last two decades of EM arrays, e.g., [44]–[51]. Superdirective EM UCAs were considered in early articles, such as [11], [52], but few have been reported recently because of the stigma attached to the concept, i.e., the notions that superdirective systems are impractical because they are ill-posed designs that are highly sensitive to component and material variations; they require unrealizable excitations; they have extremely narrow bandwidths; and they have very low radiation efficiencies.

On the other hand, superdirectivity has been demonstrated with many EM end-fire uniform linear arrays (ULAs) of electric monopoles and dipoles, e.g., [53]–[62], as well as other electric [63]–[65] and magnetic [66] based systems. Very recent explorations of superdirectivity with broadside radiating elements and arrays of them have been enabled by mixtures of electric and magnetic multipoles [67]–[70]. These multipole concepts lead to attractive optimization approaches specifically for UCAs that will be introduced later in this article.

While EM UCAs will be emphasized, there is a substantial amount of literature to be found on acoustic UCAs, most notably superdirective acoustic UCAs as receiving an-

tennas [45], [71]–[76]. Acoustic UCAs as sensing and data acquisition systems are important, e.g., for audio engineering and sonar. The eigenbeam decomposition and synthesis (EBDS) method to achieve superdirective acoustic arrays was introduced in the series of papers [77], [78]. These eigenbeams are essentially the azimuthal multipoles of the scalar (acoustic) Helmholtz equation. An eigen-beamformer (EBF) [73] employs these multipoles to expand any square-integrable function on a circle into a series of circular harmonics or eigenbeams [72] that can be combined to synthesize the coefficients of a desired pattern by Fourier transform. The EBF approach has been combined effectively with many signal processing approaches such as the MUSIC and ESPIRIT algorithms to perform all signal processing functions of a sensor UCA in its beamspace.

In this paper, Section I explores optimizing the radiated field properties of vertically-polarized (VP) UCAs from several points of view, including the acoustic EBDS method and an EM multipole-based approach, that achieve compact superdirecitve UCAs. The basics of VP dipole-based UCAs will be reviewed in Section II. The omnidirectional-mode (OM) properties of such UCAs, which consist of even and odd number of elements, will be discussed to lay the foundations for the various UCA examples to be treated. Beam-forming with their directive modes (DMs) will be described in Section III. A UCA of half-wavelength dipoles and its performance characteristics will be given; it will act as the baseline design. To achieve higher directivity in either their OM or DM states, novel semi-circular and sectoral UCAs are constructed with unidirectional Huygens dipole antennas (HDAs) [79] as their elements in Section IV. Since they are unidirectional radiators, the nuances of the HDAs pointing radially or in a specified beam direction will be examined and compared. The Rayleigh quotient (RQ) optimization method will be applied to UCAs in Section V to determine if the DM performance can be enhanced further. Several of the EM UCA cases given up to this point will be demonstrated to be superdirective. The acoustic UCA-based EBDS optimization method will then be introduced in Section VI and applied to a typical ideal, compact acoustic UCA of isotropic radiators for comparison to the performance characteristics achieved with the preceeding EM UCAs. Finally, a Bessel-azimuthal multipole (BEAM) method will be developed in Section VII. This BEAM approach will be applied to a set of UCAs of densely-packed half-wavelength VP electric dipoles and VP HDAs. It will be demonstrated that the DMs of the resulting BEAM-designed compact UCAs are also superdirective, but with superior performance characteristics when compared to the other systems. Conclusions are summarized in Section VIII.

II. Basic Analysis of a Circular Array of Dipoles

1. Dipole fields

A circular array of basic dipole elements is considered first.

Let the electric and magnetic dipoles be oriented in the $\hat{u}$ and $\hat{v}$ directions, respectively, in free space. Let their current moments and locations be $I_e\ell_e$, $I_m\ell_m$, $\vec{r}_e$ and $\vec{r}_m$, respectively. Then their electric fields in their far fields are given by the expressions [80]:

$$\vec{E}_J^{\text{ff}}(x,y,z) = j\omega\mu_0\,(I_e\,\ell_e)\,e^{+jk\,\vec{r}_e\cdot\hat{r}}\,\frac{e^{-jkr}}{4\pi r}\,(\hat{r}\times\hat{r}\times\hat{u})$$

$$\vec{E}_K^{\text{ff}}(x,y,z) = j\omega\mu_0\,(I_m\,\ell_m)\,e^{+jk\,\vec{r}_m\cdot\hat{r}}\,\frac{e^{-jkr}}{4\pi r}\,(\hat{r}\times\hat{v}) \qquad (1)$$

where $r = (x^2+y^2+z^2)^{1/2}$ and $\hat{r} = \vec{r}/r$ and $k = \omega\sqrt{\varepsilon_0\mu_0} = 2\pi/\lambda_0$, and f_0 is the operating frequency of the source so that $\omega = 2\pi f_0$ and $\lambda_0 = 1/(f_0\sqrt{\varepsilon_0\mu_0})$. Half-wavelength dipoles will also be considered since, as noted, many UCAs consist of them or their equivalent ground plane-based quarter-wavelength monopoles to achieve higher directivities. Recall that the far-field of an electric dipole of length L oriented along the $+z$-axis is [81]

$$\vec{E}_{\text{ed},L}^{\text{ff}}(r,\theta,\phi) = j\omega\mu_0 I_0 e^{+jk\,\vec{r}_e\cdot\hat{r}}\,\frac{e^{-jkr}}{4\pi r}\,\mathcal{EF}_{\text{ed},L}(\theta,\phi)\,\hat{\theta} \qquad (2)$$

where the element factor

$$\mathcal{EF}_{\text{ed},L}(\theta,\phi) = 2\left\{\frac{\cos\left[(k_0L/2)\cos\theta\right]-\cos(k_0L/2)}{\sin\theta}\right\} \qquad (3)$$

2. Array fields

The basic circular array is taken to be one with N elements, each being an ideal vertical electric dipole, i.e., each dipole is oriented along the z-axis and centered with respect to the xy-plane. Semi-circular and sectoral UCAs will also be considered throughout. An example 13-element full UCA is depicted in Figure 1(a). Similarly, example 7-element semi-circular and 60°-sector arrays are illustrated in Figures 1(b) and (c).

The far-field expression of the n-th dipole is thus

$$\vec{E}_n^{\text{ff}}(r,\theta,\phi) = j\omega\mu_0\,(I\ell)_n\,e^{+jk\,\vec{r}_n\cdot\hat{r}}\,\frac{e^{-jkr}}{4\pi r}\,(\hat{r}\times\hat{r}\times\hat{z}) \qquad (4)$$

As compiled in the Appendix A, the element vector field of this dipole is

$$\mathcal{EVF}_{\text{ed}}(\theta,\phi) = \hat{r}\times\hat{r}\times\hat{z}$$
$$= \sin\theta\cos\theta\cos\phi\,\hat{x} + \sin\theta\cos\theta\sin\phi\,\hat{y} - \sin^2\theta\,\hat{z}$$
$$= \sin\theta\,\hat{\theta} \qquad (5)$$

Because the array elements lie on a circle of radius a, the dot-product portion of the phase terms becomes

$$\vec{r}_n\cdot\hat{r} = a\,(\cos\phi_n\,\hat{x}+\sin\phi_n\,\hat{y})$$
$$\cdot(\sin\theta\cos\phi\,\hat{x}+\sin\theta\sin\phi\,\hat{y}+\cos\theta\,\hat{z})$$
$$= a\cos\phi_n\cos\phi\sin\theta + a\sin\phi_n\sin\phi\sin\theta$$
$$= a\sin\theta\cos(\phi-\phi_n) \qquad (6)$$

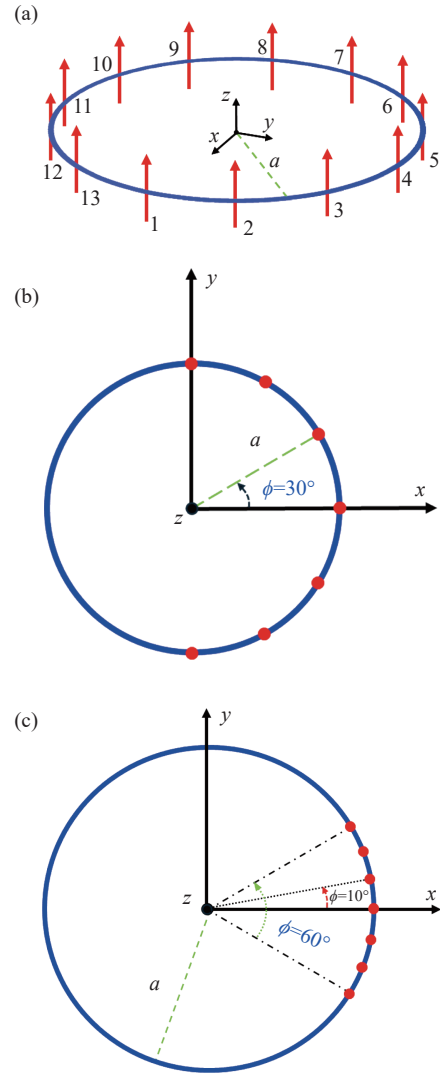and, hence, the phase terms themselves become

(a)

(b)

(c)

Figure 1 Typical UCAs to be considered in this article. (a) Full 13-element array of vertically polarized radiators; (b) 7-element semi-circular array; (c) 7-element 60°-sector array. The red dots in (b) and (c) indicate the locations of each vertically polarized radiator.

$$e^{+jk\,\vec{r}_n\cdot\hat{r}} = e^{+jka\sin\theta\cos(\phi-\phi_n)} \qquad (7)$$

To simplify the discussion and related notations, the excitation amplitudes are normalized to the value I_0 such that they are represented simply as $A_n = I_n/I_0$, for $n = 1,2,\ldots,N$. Similarly, the length of each dipole is taken to be the same: $\ell_n = \ell$. Consequently, the electric field radiated into its far field by this circular array of VP ideal electric dipoles is

$$\vec{E}_{\text{total}}^{\text{ff}}(r,\theta,\phi) = j\omega\mu_0 I_0\ell\,\frac{e^{-jkr}}{4\pi r}\,\mathcal{AF}(\theta,\phi)\times\mathcal{EVF}_{\text{ed}}(\theta,\phi) \qquad (8)$$

where the array factor

$$\mathcal{AF}(\theta,\phi) = \sum_{n=1}^{N} A_n e^{+jka\sin\theta\cos(\phi-\phi_n)} \qquad (9)$$

Furthermore, it will assumed initially that the current amplitude of each element is the same, i.e., $I_n = I_0$ so that

$A_n = 1.0$, and that the array elements are equally spaced on its circle, i.e., a full UCA is considered. It radiates an omnidirectional field. A MATLAB code was written that calculates the array factor and element vector field terms to find the directivity patterns that this omnidirectional mode (OM) of the array produces, i.e., it calculates

$$\mathcal{AP}_{OM}(\theta,\phi) = \mathcal{AF}_{OM}(\theta,\phi) \times \mathcal{EVF}_{ed}(\theta,\phi) \qquad (10)$$

where the array factor term becomes simply

$$\mathcal{AF}_{OM}(\theta,\phi) = \sum_{n=1}^{N} e^{+jka\sin\theta\cos(\phi-\phi_n)} \qquad (11)$$

Similarly, an array of half-wavelength dipoles, i.e., those with $L = \lambda/2$, is considered. Its directivity patterns follow from the analogous expression:

$$\mathcal{AP}_{OM-HW}(\theta,\phi) = \mathcal{AF}_{OM}(\theta,\phi) \times \mathcal{EVF}_{ed,hw}(\theta,\phi) \qquad (12)$$

where $\mathcal{EVF}_{ed,hw}(\theta,\phi) = \mathcal{EF}_{ed,L}|_{L=\lambda_0/2}(\theta,\phi)\,\hat{\theta}$.

3. Odd versus even number of array elements

A UCA of vertical electric dipoles provides the means to have a natural OM and associated radiated field performance in its azimuthal plane. However, the number of elements in a full UCA – whether it is even or odd – impacts the shape and quality of its pattern. This is particularly true of its out-of-roundedness (OoR) values, i.e., the differences between its radiation pattern in the azimuthal plane and a circle whose radius is the average value of that pattern over those angles. These OoR effects were studied in the early paper [3] where it was demonstrated that an odd number of elements yields superior performance characteristics. This issue is important since we would like an array that works optimally in both its OM and DM states simply by changing the excitation amplitudes. As will be demonstrated later, an odd number is also advantageous for the DM of a semicircular or sector array centered about the desired beam direction since the center element will coincide with that direction.

Examples of UCAs with 12 and 13 ideal, Hertzian dipole elements confirm the odd number outcome. The radius of the array is arbitrarily chosen to be $a = \lambda$, which means that its $ka = 2\pi$ and its perimeter $2\pi a = 6.28\,\lambda$. The 12- and 13-element UCA results are presented, respectively, in Figures 2 and 3.

The 12-element patterns in the horizontal azimuthal plane and in the two vertical principal planes are given, respectively, in Figure 2(a) and Figures 2(c) and (d). The radius of the red circle in Figure 2(a), 2.49 dB, is the average of the blue circle's values – the UCA's pattern. The latter's maximum value is 2.56 dB. The OoR values, i.e., the differences between the two curves, are summarized in Figure 2(b). The maximum OoR value is 0.07 dB, a 1.60% difference. The maximum directivity in Figures 2(c) and (d) is 3.72 dB. As Figure 2(c) shows, it is not along the azimuthal plane.

Figure 2 Calculated directivity results for the OM of the UCA with 12 vertical dipole elements and a radius giving $ka = 2\pi$. (a) Array pattern in the azimuthal xy-plane compared to the average directivity reference. (b) OoR values. Array patterns in the two principal vertical planes. (c) Linear plot. (d) Polar plot.
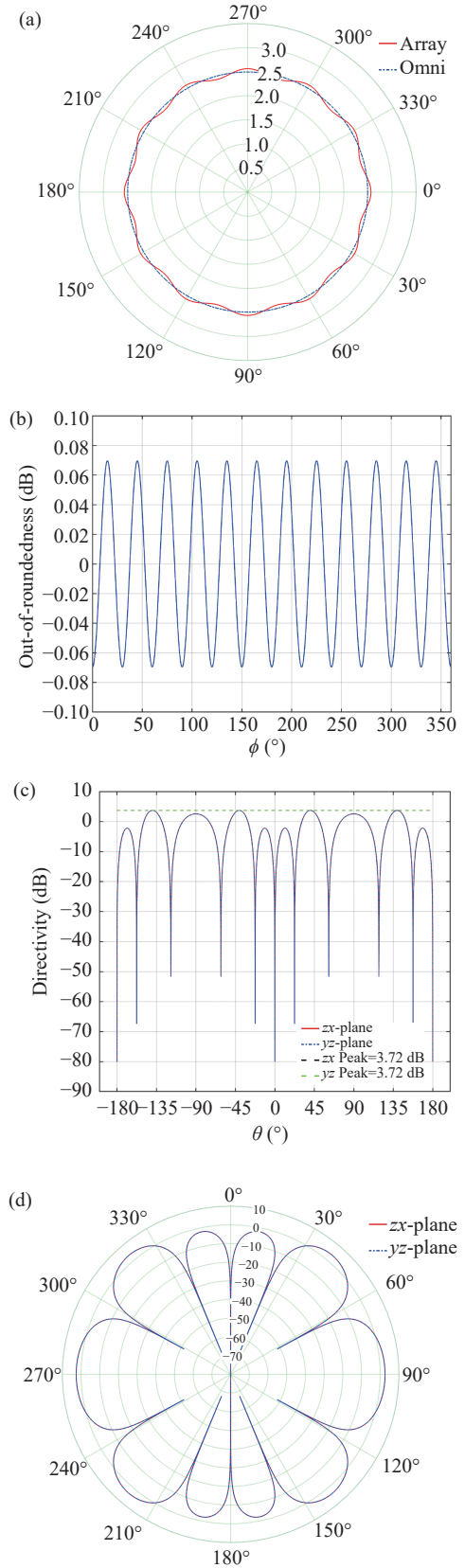
Figure 3 Calculated directivity results for the OM of the UCA with 13 vertical dipole elements and a radius giving $ka = 2\pi$. (a) Array pattern in the azimuthal xy-plane compared to the average directivity reference. (b) OoR values. Array patterns in the two principal vertical planes. (c) Linear plot. (d) Polar plot.
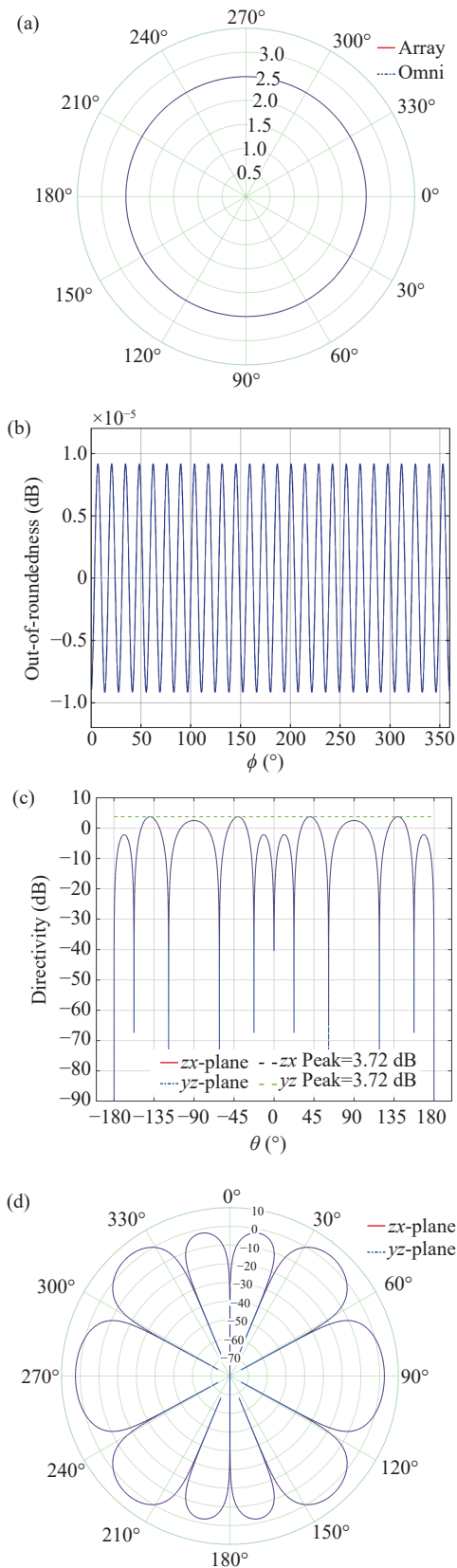
The 13-element patterns in the horizontal azimuthal plane and in the two vertical principal planes are given, respectively, in Figure 3(a) and Figures 3(c) and (d). The radius of the red circle in Figure 2(a), 2.49 dB, is the average of the blue circle's values – the UCA's pattern. The latter's maximum value is 2.49 dB, i.e., the two curves are basically coincident. The OoR values are summarized in Figure 3(b). The maximum OoR value is 9.17×10^{-6} dB, a $2.11 \times 10^{-4}\%$ difference. Thus, the odd number of elements indeed yields superior OoR values of the OM's pattern in the xy-plane. However, note in Figures 3(c) and (d) that the maximum directivity is again 3.72 dB. Moreover, as Figure 3(c) clearly shows, it too is not along the azimuthal plane.

Corresponding UCAs with 12 and 13 ideal, half-wavelength dipole elements were also considered. The results are essentially the same, but with some notable differences. The 12-element UCA yields a maximum directivity of 3.17 dB (2.075) on the horizontal plane and at $\theta = \pi/2$ for both vertical planes, i.e., on the xy-plane. Thus, the longer dipoles facilitate producing the maximum directivity along the horizontal plane. However, the average directivity value in the horizontal plane is only 3.10 dB. Therefore, the maximum OoR value, 0.07 dB, is the same as that of the Hertzian dipole-based UCA. In contrast, the 13-element UCA yields a maximum directivity of only 3.10 dB (2.043) in the horizontal plane. Nonetheless, its OoR properties are also the same as those of the corresponding Hertzian dipole-UCA, i.e., the maximum OoR value is again only $2.11 \times 10^{-4}\%$ different from the average. On the other hand, the maximum directivity is 3.14 dB (2.062) in both vertical planes. While it is not precisely along the xy-plane, it is only 0.92% different. These results again confirm the OoR superiority of an odd number of elements, but they also explain why the maximum directivity results in the horizontal and vertical planes were significantly different in the Hertzian dipole cases. The smallness of the Hertzian dipoles and their broader patterns produce significant constructive interference at large elevation angles.

III. Beam Pointing

The ability to phase a UCA to achieve a collimated beam whose maximum directivity is pointed in the direction (θ_0, ϕ_0) is another important applications feature. The simplest version is achieved by weighting the amplitudes only with progressive phase terms. The well-known expression is [7], [8], [81]

$$A_n = B_n e^{j\Psi_n} = B_n e^{-jka \sin\theta_0 \cos(\phi_0 - \phi_n)} \tag{13}$$

Comparing this phase choice with (9), the elements of the array will radiate coherently (in phase) in the specified direction. The amplitudes B_n are taken at this point to be identical and untapered, i.e., $B_n = 1.0$. If sidelobe control is desired, then the B_n would have to be defined according to the desired outcome of which there are many choices. The subsequent array factor and directivity patterns that result in this directional mode (DM) of the array are

$$\mathcal{AF}_{\mathrm{DM}}(\theta,\phi) = \sum_{n=1}^{N} B_n \times \mathrm{e}^{+jka[\sin\theta\cos(\phi-\phi_n)-\sin\theta_0\cos(\phi_0-\phi_n)]} \quad (14)$$

where for the ideal dipoles

$$\mathcal{AP}_{\mathrm{DM,ed}}(\theta,\phi) = \mathcal{AF}_{\mathrm{DM}}(\theta,\phi) \times \mathcal{EVF}_{\mathrm{ed}}(\theta,\phi) \quad (15)$$

and for the half-wavelength dipoles

$$\mathcal{AP}_{\mathrm{DM,hw}}(\theta,\phi) = \mathcal{AF}_{\mathrm{DM}}(\theta,\phi) \times \mathcal{EVF}_{\mathrm{ed,hw}}(\theta,\phi) \quad (16)$$

The directivity patterns for a specified maximum direction, which is taken to be $(\theta_0 = \pi/2, \phi_0 = 0)$ simply as an example, were obtained with another MATLAB code. They are presented in Figure 4 for the 13-element UCA of half-wavelength vertical dipoles. It can be readily confirmed in Figures 4(a) and (c) that the maximum directivity in the horizontal xy-plane and the principal vertical zx-plane is 12.67 dB in the specified direction. The backlobe level is 3.68 dB yielding a front-to-back ratio (FTBR) of only 8.99 dB. The first sidelobe level in the xy-plane is 4.77 dB, only -7.90 dB below the peak value. The maximum directivity in the orthogonal yz-plane is -3.68 dB. The corresponding polar plots of the directivity patterns are given in Figures 4(c) and (d).

IV. Arrays of Vertically Polarized Huygens Dipole Antennas (HVP)

With the desire to enhance the directivity of the array, it was felt that using unidirectional HDAs [79], [82]–[87] could avoid radiated energy being wasted in the back direction when vertical dipoles are used to form the UCA without any additional structures to recover it. A linearly polarized (LP) HDA is formed with two orthogonal current moments, an electric and a magnetic one that are in-phase and in balance, which create radiated far fields of equal magnitude. The LP nature of the fields is along the electric current direction.

In analogy with the dipole array, let the electric dipole element of the HDA be oriented along the $+z$-axis, $\hat{e}_d = +\hat{z}$. It is then VP along the z-axis, and the magnetic dipole element lies in the xy-plane. Moreover, the HDA's unidirectional field will then have its maximum along the xy-plane. Therefore, because the array is on a circle in the xy-plane, the array's maximum beam direction will also be along the xy-plane. In fact, one could consider the ultra-thin Huygens dipole antenna array developed in [80] as a replacement for the single dipole radiator and orient the plane of the array along the z-axis to act as a subarray of the UCA. This multilayer along-the-z-axis configuration would offer beam scanning in the elevation plane. However, in either the single or multi-element case, there is then a choice. One could have the maximum radiated field direction of each HDA be along the radial direction or point in a specified direction. Consequently, the potential improvement of the UCA's directivity is considered in two cases, i.e., when the unidirec-
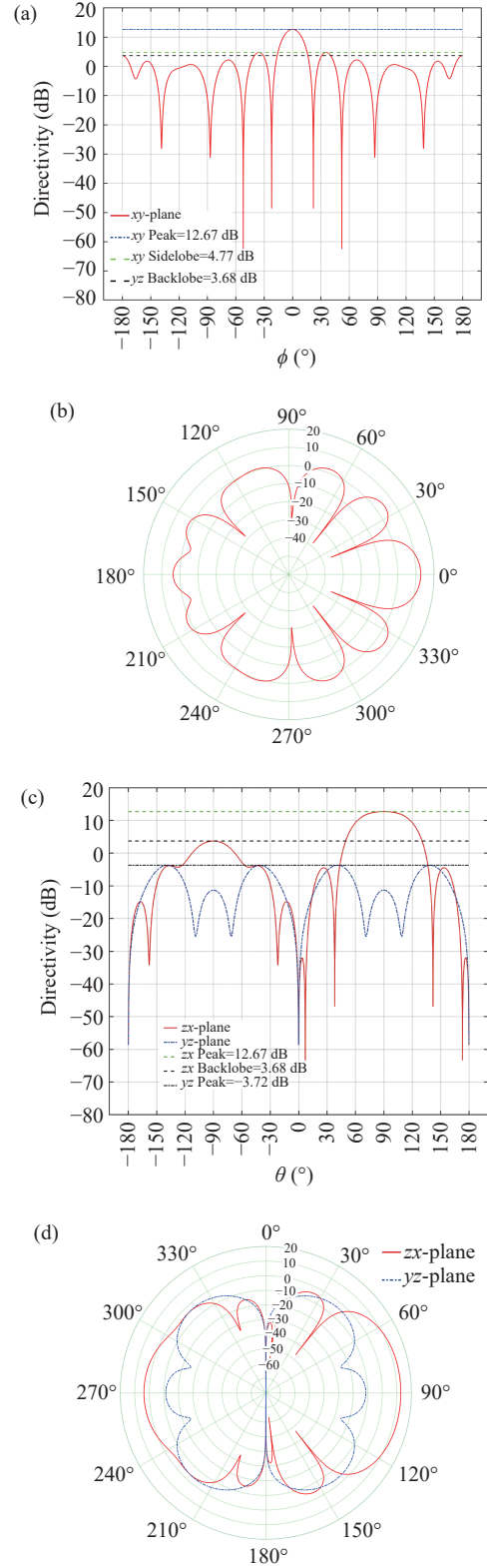

Figure 4 Calculated directivity results of the basic DM of the UCA with 13 vertical half-wavelength dipole elements and a radius giving $ka = 2\pi$. Horizontal xy-plane: (a) Linear plot and (b) Polar plot. Two principal vertical (zx and yz) planes: (c) Linear plot and (d) Polar plot.

tional fields of the HDA elements are pointed in the radial direction corresponding to their location in the array or when they are all pointed in the same specified direction.

1. Each element points in its radial direction

If each VP HDA, now denoted throughout as a HVP, is to be pointed in the radial direction corresponding to its position in the UCA, then its maximum direction is identified by the angles $(\theta,\phi) = (\pi/2,\phi_n)$. With the electric dipole element being oriented along the $+z$-axis, this configuration then requires the magnetic dipole element to be oriented along the $-\hat{\phi}(\pi/2,\phi_n)$ direction in the xy-plane. From the Appendix A, this means the magnetic dipole element vector should be $\hat{m}_d = \sin\phi_n\hat{x} - \cos\phi_n\hat{y}$. Therefore, the requisite Huygens cross-product direction is correct: $\hat{e}_d \times \hat{m}_d = \cos\phi_n\hat{x} + \sin\phi_n\hat{y} = \hat{r}(\theta=\pi/2,\phi_n)$. A representative 7-element semi-circular UCA of radially-directed HVPs is depicted in Figure 5.
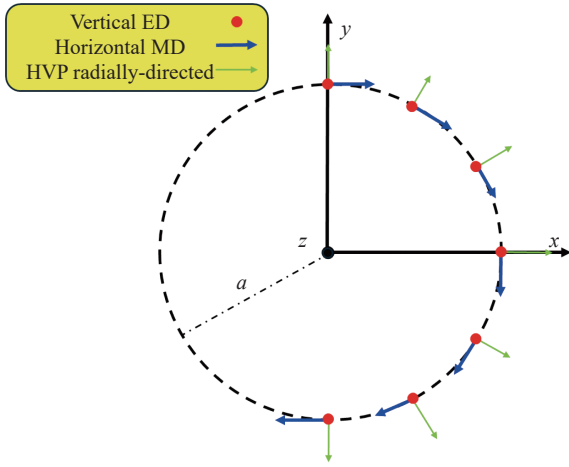

Figure 5 7-element semi-circular UCA of radially-directed HVPs.

The UCA's directivity then follows from the HVP's element vector field:

$$\vec{\mathcal{P}}(\theta,\phi) = \hat{r}\times\hat{r}\times\hat{z} + \hat{r}\times(\sin\phi_n\hat{x} - \cos\phi_n\hat{y}) \quad (17)$$

The unit vector terms are obtained with the expressions in the Appendix A to yield

$$\begin{aligned}\vec{\mathcal{P}}(\theta,\phi) = &\cos\theta[\sin\theta\cos\phi - \cos\phi_n]\,\hat{x}\\ &+ \cos\theta[\sin\theta\sin\phi - \sin\phi_n]\,\hat{y}\\ &- \sin\theta[\sin\theta + \cos(\phi - \phi_n)]\,\hat{z}\end{aligned} \quad (18)$$

As a check, one finds

$$\vec{\mathcal{P}}(\theta=\pi/2,\phi) = -[1 + \cos(\phi - \phi_n)]\,\hat{z} \quad (19)$$

which is correct, i.e., it is a cardioid shape with its maximum in the $\phi = \phi_n$ direction. In particular, the element vector field is $-2\hat{z}$ for $\phi = \phi_n$ and 0 for $\phi = \phi_n + \pi$. Recall that because the electric dipoles are oriented along the $+z$-direction, their fields in the xy-plane are along the $-z$-direction. Consequently, its magnitude squared (power pattern) in the xy-plane also exhibits the cardioid shape with its peak along the $\phi = \phi_n$ direction, i.e., the direction broadside to the electric and magnetic dipole elements:

$$|\vec{\mathcal{P}}(\theta,\phi)|^2 = [1 + \cos(\phi - \phi_n)]^2 \quad (20)$$

Therefore, the FTBR of the power patterns is $|\vec{\mathcal{P}}(\theta = \pi/2, \phi = \phi_n)|^2/|\vec{\mathcal{P}}(\theta = \pi/2, \phi = \phi_n + \pi)|^2 = \infty$.

2. Each HVP points at the direction specified for the DM

On the other hand, let the desired maximum direction of the beam produced by the entire array in the xy-plane be $(\theta,\phi) = (\pi/2,\phi_{\max})$. We then consider the maximum direction of the HDA at each $(\theta,\phi) = (\pi/2,\phi_n)$ to be this desired direction: $(\theta_{\max},\phi_{\max}) = (\pi/2,\phi_{\max})$. This in turn requires the magnetic dipole element to be oriented along $-\hat{\phi}(\pi/2,\phi_{\max})$ in the xy-plane. From the Appendix A, this means the magnetic dipole element vector should be $\hat{m}_d = \sin\phi_{\max}\hat{x} - \cos\phi_{\max}\hat{y}$. Therefore, the requisite Huygens cross-product direction is correct: $\hat{e}_d \times \hat{m}_d = \cos\phi_{\max}\hat{x} + \sin\phi_{\max}\hat{y} = \hat{r}$ $(\theta = \pi/2,\phi_{\max})$. A representative 7-element semi-circular UCA of max-directed HVPs is depicted in Figure 6.
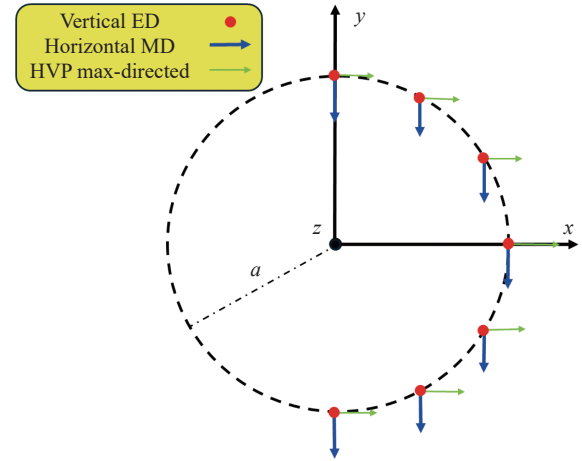

Figure 6 7-element semi-circular UCA of max-directed HVPs.

The MATLAB code thus needs the HVP's element vector field:

$$\vec{\mathcal{P}}(\theta,\phi) = \hat{r}\times\hat{r}\times\hat{z} + \hat{r}\times(\sin\phi_{\max}\hat{x} - \cos\phi_{\max}\hat{y}) \quad (21)$$

The unit vector terms are again obtained from the expressions in Appendix A to yield

$$\begin{aligned}\vec{\mathcal{P}}(\theta,\phi) = &\cos\theta[\sin\theta\cos\phi - \cos\phi_{\max}]\,\hat{x}\\ &+ \cos\theta[\sin\theta\sin\phi - \sin\phi_{\max}]\,\hat{y}\\ &- \sin\theta[\sin\theta + \cos(\phi - \phi_{\max})]\,\hat{z}\end{aligned} \quad (22)$$

As a check, one finds

$$\vec{\mathcal{P}}(\theta=\pi/2,\phi) = -[1 + \cos(\phi - \phi_{\max})]\,\hat{z} \quad (23)$$

which is correct, i.e., it is a cardioid shape with maximum in the $\phi = \phi_{\max}$ direction. In particular, the element vector field is $-2\hat{z}$ for $\phi = \phi_{\max}$ and 0 for $\phi = \phi_{\max} + \pi$. Recall again that because the electric dipoles are oriented along the $+z$-direction, their fields in the xy-plane are along the $-z$-

direction.

Consequently, its power pattern, which is magnitude squared of (23), in the xy-plane also exhibits the cardioid shape with its peak along the $\phi = \phi_{\max}$ direction, i.e., the direction broadside to the electric and magnetic dipole elements:

$$|\vec{\mathcal{P}}(\theta,\phi)|^2 = [1 + \cos(\phi - \phi_{\max})]^2 \qquad (24)$$

Therefore, the power patterns' FTBR is $|\vec{\mathcal{P}}(\theta = \pi/2, \phi = \phi_{\max})|^2 / |\vec{\mathcal{P}}(\theta = \pi/2, \phi = \phi_{\max} + \pi)|^2 = \infty$.

3. Comparison results

One immediate issue arose when the first radial cases were simulated. Because the array is circular, the magnetic dipoles on one semi-circle of the array are oriented opposite to those on the other one. Thus, there is a cancellation of the overall magnetic dipole fields, much like what occurs when an electric dipole is oriented parallel to a ground plane and near to it. This outcome ruins the advantage of the HVPs for the OM. On the other hand, the DM of an UCA is typically accomplished with only a limited number of its elements. Consequently, only semi-circular and sectoral arrays of HVPs oriented along their radial position are considered.

Semi-circular arrays consisting of seven Hertzian and seven half-wavelength dipoles are simulated first as reference cases. These arrays extend from $\phi = -90°$ to $\phi = +90°$ with 30° separation between each element. The array size remains $ka = 2\pi$ and the desired maximum direction is again taken to be along the x-axis: $(\theta_{\max}, \phi_{\max}) = (\pi/2, 0)$, in both cases.

The calculated patterns of the Hertzian dipole case are shown in Figures 7(a) and (b). The peak directivity in both the vertical plane along the beam direction (zx-plane) and the horizontal xy-plane is 9.96 dB along the specified beam direction $(\theta_{\max}, \phi_{\max}) = (90°, 0°)$. The corresponding backlobe is 7.33 dB, yielding a poor FTBR of 2.63 dB. The peak directivity in the orthogonal vertical (yz) plane is -3.09 dB. The calculated patterns of the half-wavelength dipole case are shown in Figures 7(c) and (d). The peak directivity in both the vertical zx-plane and the horizontal xy-plane is 10.32 dB along the specified beam direction $(\theta = 90°, \phi = 0°)$. The corresponding backlobe is 7.70 dB, yielding the same poor FTBR of 2.63 dB. The first sidelobe level is 3.94 dB, only -6.38 dB below the maximum value. The peak directivity in the orthogonal vertical (yz) plane is -2.89 dB.

The calculated patterns of the corresponding semi-circular array of seven radially-directed HVPs are shown in Figure 8. The peak directivity in both the vertical zx-plane and the horizontal xy-plane is 11.03 dB along the specified beam direction $(\theta = 90°, \phi = 0°)$. This peak value is 0.71 (1.07) dB larger than the half-wavelength (Hertzian) dipole case. The corresponding backlobe is -0.09 dB, yielding a significantly improved FTBR of 11.12 dB. The first sidelobe level is 1.03 dB, -10.00 dB below the maximum value. The peak directivity in the orthogonal vertical (yz) plane is
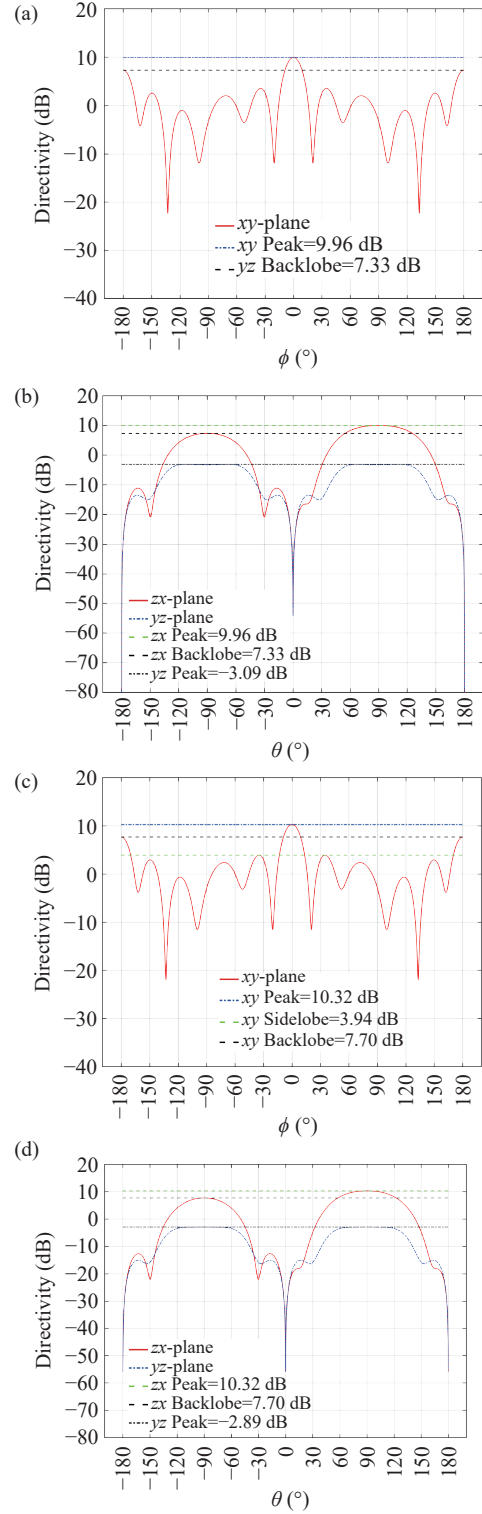
Figure 7 Calculated directivity results of the semi-circular array of seven elements with $ka = 2\pi$. Hertzian dipoles: (a) Horizontal, xy-plane, and (b) Two principal vertical planes. Half-wavelength dipoles: (c) Horizontal, xy-plane, and (d) Two principal vertical planes.

-3.08 dB.

The DM of a UCA is most often realized with only a set of its elements being excited over an angular sector. An example is the multi-ring system reported in [5]. The reference sector array consists of seven half-wavelength dipoles
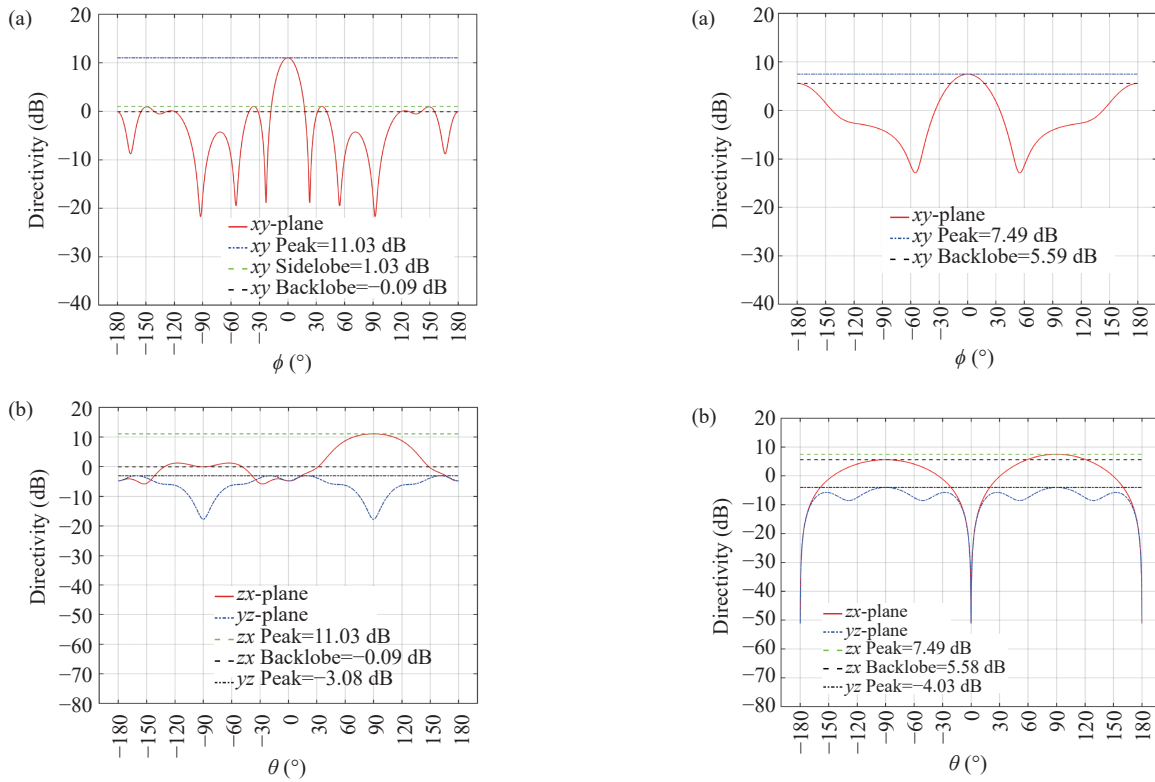
(a)

(b)

Figure 8 Calculated directivity results of the semi-circular array of seven radially-directed HVPs with $ka = 2\pi$. (a) Horizontal, azimuthal plane. (b) Two principal vertical planes.

spanning a 60° arc, i.e., the array extends from $\phi = -30°$ to $\phi = +30°$ with 10° separation between each element. The calculated patterns are given in Figures 9(a) and (b). The peak directivity in both the vertical zx-plane and the horizontal xy-plane is 7.49 dB along the specified beam direction ($\theta = 90°, \phi = 0°$). The corresponding backlobe is 5.58 dB, yielding a very poor FTBR of 1.91 dB. The peak directivity in the orthogonal vertical (yz) plane is −4.03 dB.

The calculated patterns of the corresponding sector array of seven radially-directed HVPs are shown in Figures 9(c) and (d). The peak directivity in both the vertical zx-plane and the horizontal xy-plane is 8.58 dB along the specified beam direction ($\theta = 90°, \phi = 0°$). This peak value is 1.09 dB larger than the half-wavelength dipole case. The corresponding backlobe is −22.82 dB, yielding a FTBR of 31.40 dB, which is significantly better in comparison to those values of that case. The first sidelobe level is −12.25 dB, −20.83 dB below the maximum value. There really is no definitive sidelobe in the comparison case because of its very high backlobe value. The peak directivity in the orthogonal vertical (yz) plane is 1.84 dB. The fact that the FTBR value is significantly better than any of the other cases arises from the unidirectional nature of the HVPs.

The results clearly indicate that there are benefits to utilizing HVPs as the array elements for both the semi-circular and sector arrays. Nevertheless, what would be the benefit if, in fact, all the HVPs had their maximum beam direction pointed to the specified maximum direction? To

(a)

(b)

(c)

(d)

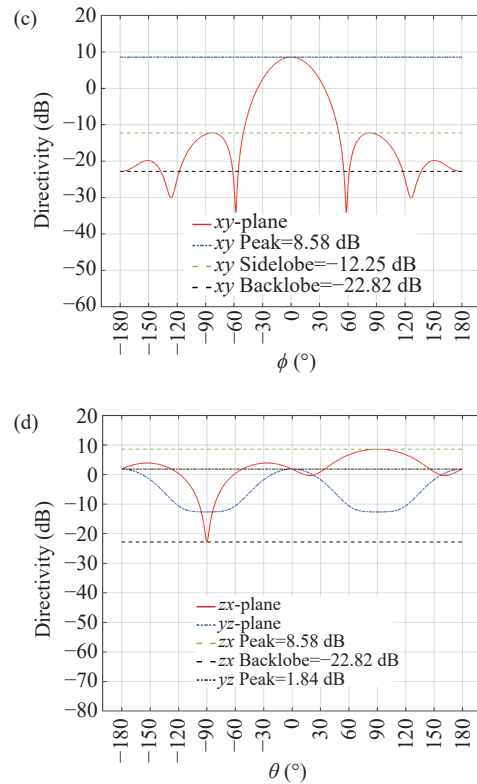**Figure 9** Calculated directivity results of the 60°-sector arrays of seven elements with $ka = 2\pi$. (a) Half-wavelength dipoles, horizontal plane. (b) Half-wavelength dipoles, two principal vertical planes. (c) Radially-directed HVPs, horizontal plane. (d) Radially-directed HVPs, two principal vertical planes.

examine this issue, both the same semi-circular and sector array configurations were examined with each HVP point-

ing in the desired maximum direction along the x-axis: $(\theta_{max}, \phi_{max}) = (\pi/2, 0)$. The calculated results are presented in Figure 10.

The semi-circular array results are shown in Figures 10 (a) and (b). The peak directivity in both the vertical zx-plane and the horizontal xy-plane is 12.13 dB along the specified beam direction ($\theta = 90°, \phi = 0°$). The corresponding backlobe level is −314.76 dB, yielding a FTBR of 326.89 dB. The first sidelobe level is 4.94 dB, −7.19 dB below the maximum value. The 60°-sector array results are shown in Figures 10(c) and (d). The peak directivity in both the vertical zx-plane and the horizontal xy-plane is 8.71 dB along the specified beam direction ($\theta = 90°, \phi = 0°$). The corresponding backlobe level is −317.46 dB, yielding a FTBR of 326.17 dB. The only sidelobe level is −8.56 dB, −17.27 dB below the maximum value.

These results demonstrate that the unidirectionality of the radiated fields of the DM and their peak directivity value can be further enhanced by using HVPs pointed in the desired beam direction. Direct comparisons of the directivity patterns in the horizontal and vertical planes of both the radially- and max-directed HVPs are given in Figure 11. In contrast to Figure 11(a), Figure 11(c) clearly displays a much deeper null in the back direction which follows immediately from each HVP being pointed to radiate unidirectionally towards the desired beam direction of the array. On the other hand, the array of radially-directed HVPs has a lower sidelobe level. This occurs because the radially-directed elements on the outer edge of the array are radiating more power towards the back hemisphere whereas those of the max-directed HVPs are radiating more along the y-axis yielding the higher sidelobe level. Nevertheless, the differences are not large except for the drastically enhanced FTBR of the max-directed HVP array. Either sector array of HVPs leads to quite acceptable DM performance.

4. Tapered excitations

Tapering of the excitation amplitudes is a standard approach to suppressing the sidelobe levels of the fields radiated by an array. Simply to understand the impact of such tapering on the HVP-based sector arrays, the well-known binomial weighting of the excitation coefficients [81], [88] is applied to a radially-directed HVP sector array. In particular, the array size is increased to $ka = 6\pi$ and a 120°-sector with 21 HVPs centered with respect to the x-axis is considered with and without the binomial weighting.

The calculated directivity patterns of these sector arrays are presented in Figure 12. The uniform excitation results are shown in Figures 12(a) and (b). The maximum directivity, 15.19 dB, is along the x-axis. The first sidelobe level is 3.53 dB (−11.66 dB down from the peak). The backlobe level is −22.03 dB, yielding a FTBR of 37.22 dB. The corresponding binomial-weighted excitation results are shown in Figures 12(c) and (d). The maximum directivity, 11.21 dB, is along the x-axis. There are two sidelobes in the back hemisphere that are −36.21 dB down from the peak (at a −25.00 dB level). The backlobe level is −36.62 dB, yield-
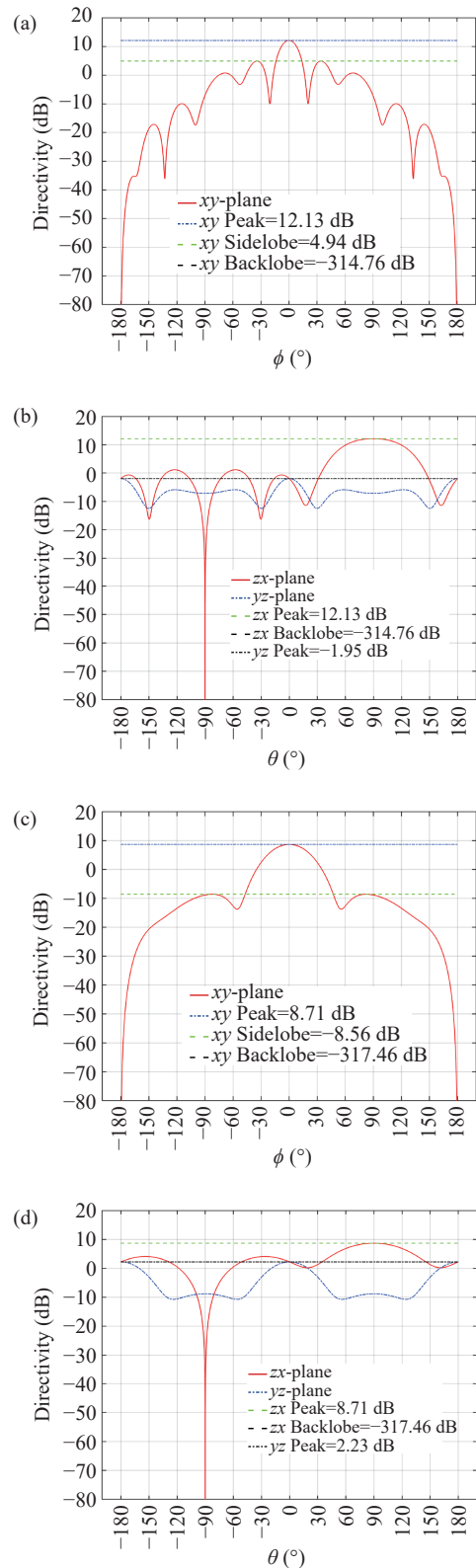
Figure 10 Calculated directivity results of the semi-circular and 60°-sector arrays with $ka = 2\pi$ and seven HVPs whose beams point in the specified beam direction of the array $(\theta_{max}, \phi_{max}) = (\pi/2, 0)$. (a) Semi-circular, horizontal plane. (b) Semi-circular, two principal vertical planes. (c) Sector, horizontal plane. (d) Sector, two principal vertical planes.

ing a FTBR of 47.83 dB. The number of sidelobes and their levels have been significantly reduced with the amplitude
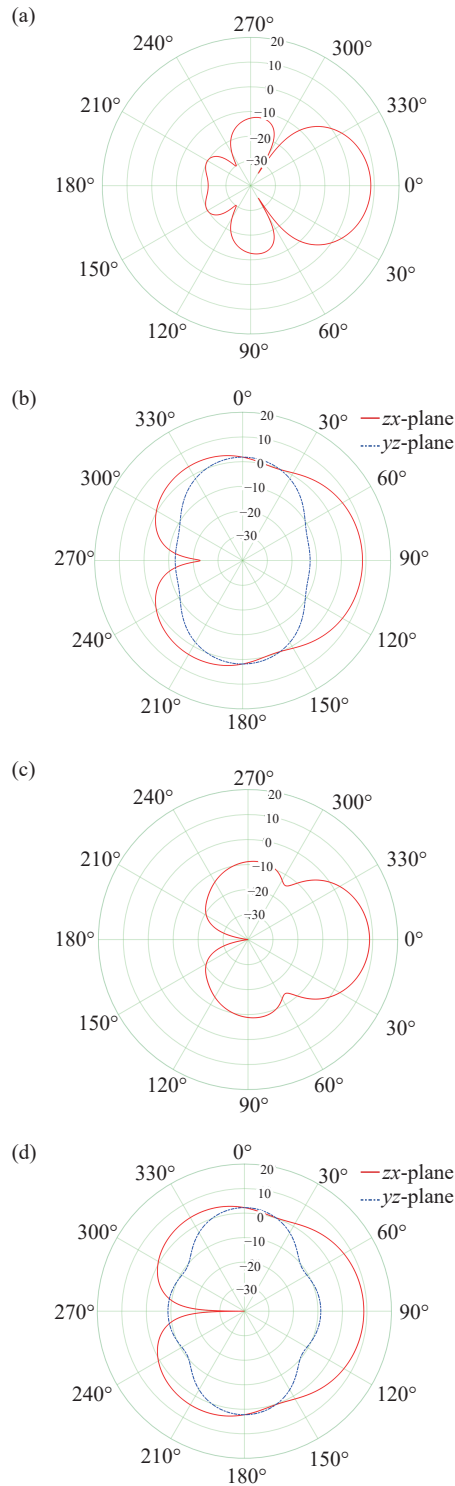
Figure 11 Calculated directivity patterns of the 60°-sector arrays of seven HVPs with $ka = 2\pi$ whose beams point in the specified direction $(\theta_{max}, \phi_{max}) = (\pi/2, 0)$. (a) Radially-directed HVPs, horizontal plane. (b) Radially-directed HVPs, two principal vertical planes. (c) Max-directed HVPs, horizontal plane. (d) Max-directed HVPs, two principal vertical planes.

Figure 12 Calculated directivity patterns of the 120°-sector arrays with $ka = 6\pi$ and 21 radially-directed HVPs centered with respect to the specified beam direction of the DM $(\theta_{max}, \phi_{max}) = (\pi/2, 0)$. (a) No taper, xy-plot (b) No taper, polar plot. (c) Binomial taper, xy-plot. (d) Binomial taper, polar plot.

tapering. However, it is with the expected cost of a decrease (26.20%) in the peak directivity and a wider main beam width. For comparison purposes, the binomial-weighted 7 HVP, $ka = 2\pi$, 60°-sector array has a 6.64 dB

maximum directivity (23.77% smaller than the uniform excitation case), no sidelobes in the horizontal and principal vertical planes, and a FTBR of 39.97 dB.

The related HVP sector arrays with the elements pointing in the specified direction were also simulated. The results are similar in the forward hemisphere, but quite different in the back hemisphere. With no tapering, the maximum directivity is along the x-axis and a tiny bit larger: 15.22 dB. The first sidelobe level is a bit higher 4.93 dB, now only −10.29 dB down from the peak. On the other hand, the backlobe level is −321.96 dB, yielding a FTBR of 337.18 dB. In contrast to the radially-directed case, there are no definitive sidelobes in the back hemisphere. However, there is a slight penalty in that those field levels are only below −2.96 dB. Similarly, with tapering the maximum directivity, 11.33 dB, is along the x-axis, again a bit larger. The backlobe level is −321.96 dB, yielding a slightly smaller FTBR of 327.91 dB. On the other hand, the two sidelobes in the back hemisphere are only 29.52 dB down from the peak (−18.19 dB level). The outcomes of either HVP element are quite attractive.

V. Rayleigh Quotient Optimization

The unconstrained Rayleigh quotient (RQ) optimization [50], [51], [53], [59], [61], [89]–[94] and its unidirectional-constrained version developed in [70] were applied to the UCAs of half-wavelength dipoles. The calculated results for the 13 element, $ka = 2\pi$ full UCA with the unconstrained RQ optimization approach and the specified direction again being along the x-axis are shown in Figures 13(a) and (b). The maximum directivity is 12.92 dB in the xy- and zx-planes. The backlobe level is 5.52 dB, yielding a small FTBR of 7.40 dB. The maximum directivity in the yz-plane is −1.60 dB.

The correspnding constrained results are shown in Figures 13(c) and (d). The FTBR constraint in the modified RQ algorithm was set to −100 dB. The maximum directivity is 12.04 dB in the xy- and zx-planes. The backlobe level is −87.96 dB, yielding a very large FTBR of 100.00 dB. The largest sidelobe in the xy-plane is 3.76 dB, almost −8.28 dB below the maximum value. The maximum directivity in the yz-plane is −5.30 dB. The cost of the substantially larger FTBR is only a 6.81% decrease in the peak directivity.

For comparison purposes, the related semi-circular and 60°-sector, 7-element half-wavelength dipole arrays with $ka = 2\pi$ were also considered. The unconstrained RQ approach applied to the semi-circular case produced a maximum of 10.26 dB along the x-axis. The backlobe level was 7.81 dB, yielding a poor FTBR of 2.45 dB. The yz-plane peak was −5.36 dB. The constrained version gave a 6.62 dB maximum with a backlobe of −93.38 dB, yielding a FTBR of 100.00 dB. The largest sidelobe in the xy-plane is 2.08 dB, which is −4.54 dB below the maximum value. The yz-peak (peak directivity in the yz-plane, which is orthogonal to the specified beam direction) was 2.28 dB. The unconstrained RQ approach applied to the same 60°-sector case produced a maximum of 9.92 dB along the x-axis. The backlobe level was −3.03 dB, yielding a FTBR of 12.95 dB. The largest sidelobe in the xy-plane is 4.23 dB, which is
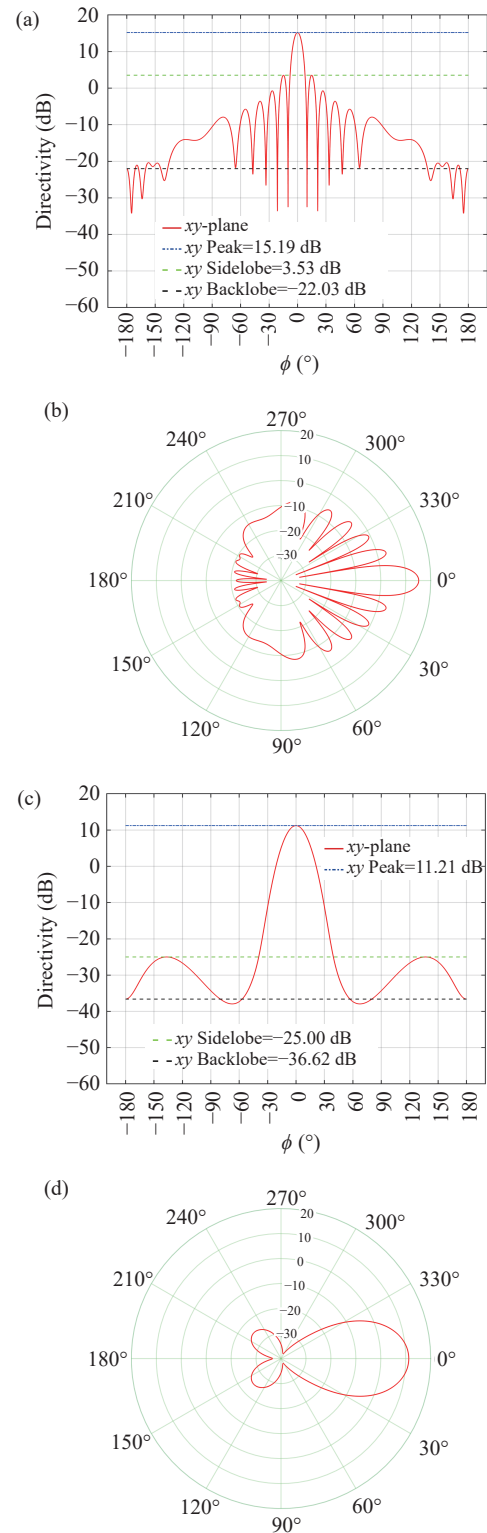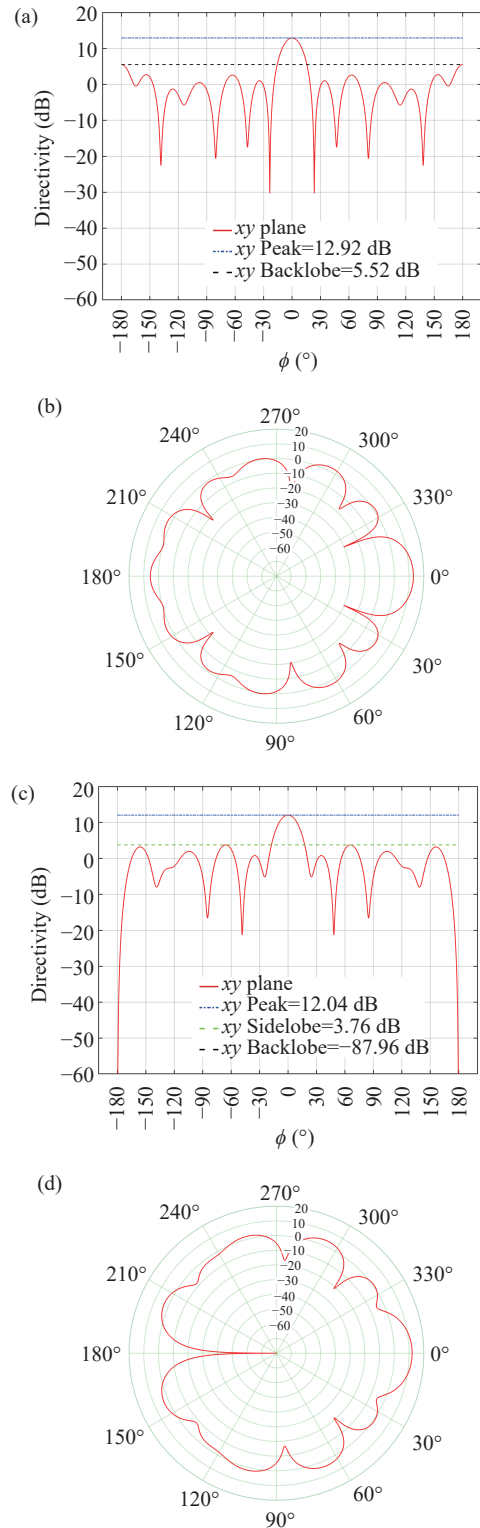

Figure 13 DM directivity patterns of the 13-element UCA of half-wavelength dipoles with $ka = 2\pi$ with specified beam direction DM $(\theta_{max}, \phi_{max}) = (\pi/2, 0)$ calculated with the RQ optimization approaches. (a) Unconstrained, xy-plot (b) Unconstrained, polar plot. (c) Constrained, xy-plot. (d) Constrained, polar plot.

−5.69 dB below the maximum value. The yz-plane peak was −3.20 dB. The constrained version gave a 9.69 dB maximum with a backlobe of −90.31 dB, yielding a FTBR

of 100.00 dB. The largest sidelobe in the xy-plane is 5.33 dB, which is −4.36 dB below the maximum value. The yz-peak was −1.78 dB. The maximum directivity values of the sector cases are larger than those of the semi-circular ones. This difference arises from the fact that the same number of dipoles are closer together in the sector case and, hence, the optimization can yield amplitude coefficients that better reinforce the fields in the specified direction.

The unconstrained RQ optimization of the semi-circular and 60°-sector 7-element max-directed HVP UCAs was also considered. It was not necessary to consider the constrained case given the unidirectional nature of the HVPs. The calculated directivity patterns in the horizontal plane of both cases are shown in Figure 14. The semi-circular case in Figures 14(a) and (b) has a maximum directivity of 12.38 dB along the x-axis with a backlobe level of −313.22 dB, which yields the FTBR = 325.60 dB. The first sidelobe level is 3.70 dB, −8.68 dB below the maximum. The largest sidelobe level in the back hemisphere is −7.15 dB, −19.53 dB below the maximum. The yz-peak was 0.11 dB. The 60°-sector case in Figures 14(c) and (d) has a maximum directivity of 11.70 dB along the x-axis with a backlobe level of −322.53 dB, which yields the FTBR = 334.24 dB. The first sidelobe level is 4.42 dB, −7.28 dB below the maximum. The largest sidelobe level in the back hemisphere is −3.04 dB, −14.74 dB below the maximum. And the yz-peak was −0.46 dB.

1. Initial summary

Several different types of UCAs and their performance characteristics have been described up to this point. The well-known definition [81] of the maximum directivity of a three-dimensional (3D) array that is uniformly excited is

$$D_{3D,max} = \frac{4\pi A_{eff}}{\lambda_0^2} \qquad (25)$$

where A_{eff} is the effective area of the array. The corresponding definition of the maximum directivity of a two-dimensional (2D) radiating system was given in [95]:

$$D_{2D,max} = \frac{2\pi W_{eff}}{\lambda_0} \qquad (26)$$

where W_{eff} is the effective width of the system. A superdirective 3D or 2D array is one whose maximum directivity exceeds, respectively, (25) or (26).

Herein, because the UCA Hertzian dipole and HVP examples are all a single layer centered about the azimuthal plane and the maximum of their DMs was designed to be in that plane, the 2D definition will be used to determine if any of those various arrays considered to this point are superdirective. Consequently, W_{eff} is taken to be twice the radius of the UCA. For instance, the arrays with $ka = 2\pi$, one then has $W_{eff} = 2\lambda_0$. Thus, one obtains $D_{2D,max} = 4\pi = 10.99$ dB (12.57). On the other hand, the arrays of half wavelength dipoles are considered to be 3D systems. Their effective area follows from the effective width of the array, W_{eff},
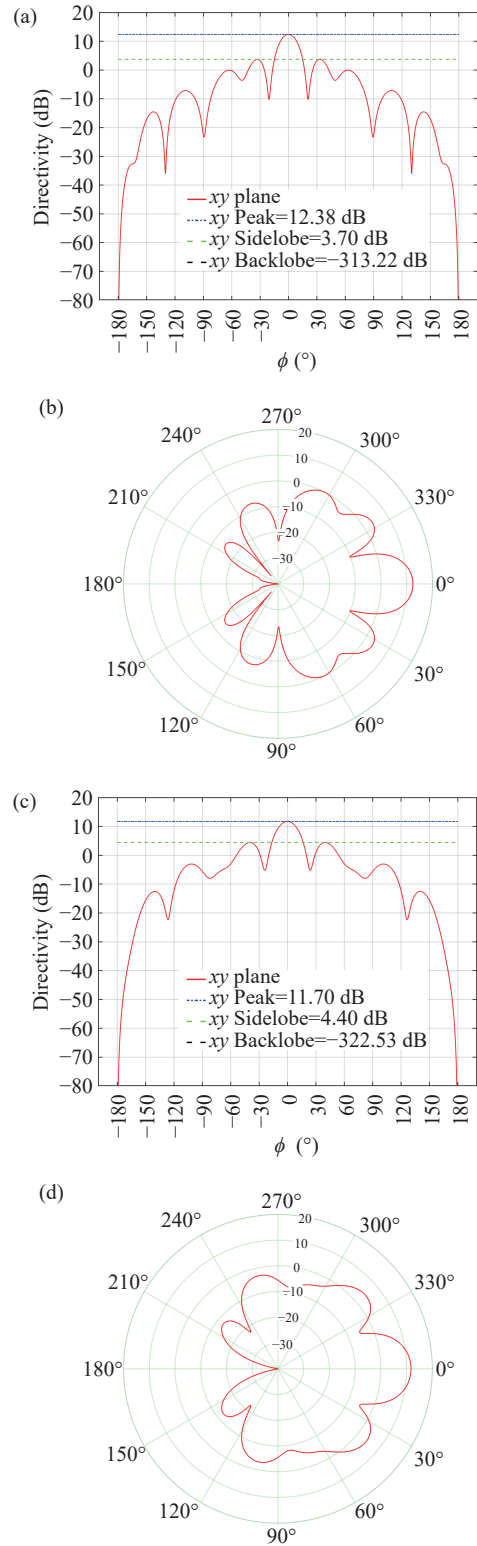
Figure 14 Calculated unconstrained RQ optimization directivity results in the horizontal planes of the semi-circular and 60°-sector arrays of seven max-directed HVPs with $ka = 2\pi$. (a) Semi-circular, linear plot. (b) Semi-circular, polar plot. (c) 60°-sector, linear plot. (d) 60°-sector, polar plot.

and its effective height H_{eff}. Then, for example, the UCAs of half-wavelength dipoles with $ka = 2\pi$ have an effective area: $W_{eff} = 2a = 2\lambda_0$ times $H_{eff} = \lambda_0/2$ equals $A_{eff} = \lambda_0^2$ and

the maximum directivity bound is $D_{\mathrm{max,3D}} = 4\pi A_{\mathrm{eff}}/\lambda_0^2 = 4\pi = 10.99$ dB (12.57). Note that it is the same as the corresponding 2D value.

Table 1 summarizes the calculated performance characteristics of the various arrays considered up to this point. It is found that the non-optimized DM and the RQ-optimized versions of the full half-wavelength UCA are superdirective. Similarly, the non-optimized and unconstrained RQ-optimized semi-circular HVP arrays are also clearly superdirective. However, the corresponding semi-circular half-wavelength dipole arrays are not.

On the other hand, the sector arrays have different effective widths and, hence, different comparison values must be determined. The effective width of the non-tapered, 120°-sector radially-directed HVP case with $ka = 6\pi$ is $W_{\mathrm{eff}} = 2a\sin(120°) = 5.2\lambda_0$ so that $D_{\mathrm{2D,max}} = 10.4\pi = 15.14$ dB. Thus, it is superdirective. Similarly, the effective width of the 60°-sector cases with $ka = 2\pi$ is $W_{\mathrm{eff}} = 2a\sin(60°) = \lambda_0$

so that $D_{\mathrm{2D,max}} = 2\pi = 7.98$ dB. Consequently, the non-optimized and RQ-optimized 60°-sector radially-directed and max-directed HVP arrays are all superdirective. Morever, the 60°-sector half-wavelength dipole arrays with $ka = 2\pi$ are superdirective as well, i.e., with their effective area $A_{\mathrm{eff}} = 0.5\lambda_0^2$, their peak directivity values are greater than $D_{\mathrm{max,3D}} = 2\pi = 7.98$ dB.

Furthermore, it is noted that if the HDA developed in [80] was used for the HVPs, its length along the z-axis would be $\lambda_0/3$. With $ka = 2\pi$ the effective area of that the semi-circular (60°-sector) array would be $A_{\mathrm{eff}} = 0.67\lambda_0^2$ ($A_{\mathrm{eff}} = 0.335\lambda_0^2$). Therefore, the corresponding maximum directivities are, respectively, $D_{\mathrm{max,3D}} = 9.23$ dB (8.38) and $D_{\mathrm{max,3D}} = 6.22$ dB (4.19). Hence, all of the semi-circular and 60°-sector radially- and max-directed HVP arrays with this HDA as their element would also be superdirective.

Finally, despite their infinitesimal height, the performance characteristics of the superdirective semi-circular

Table 1 Summary of uniform circular array results

UCA type	Mode	Element type	No. elements	ka	D_{max} (dB)	Peak dir. (dB)	FTBR (dB)	Sidelobe (dB)
Full	Omni	Hertzian dipoles	13	2π	10.99	2.49	0.0	–
Full	Omni	Half-wavelength dipoles	13	2π	10.99	3.14	0.0	–
Full	DM	Half-wavelength dipoles	13	2π	10.99	12.67	8.99	4.77
Semi-circular	DM	Hertzian dipoles	7	2π	10.99	9.96	2.63	–
Semi-circular	DM	Half-wavelength dipoles	7	2π	10.99	10.32	2.63	3.94
Semi-circular	DM	radially-directed HVPs	7	2π	10.99	11.03	11.12	1.03
Semi-circular	DM	max-directed HVPs	7	2π	10.99	12.13	326.89	4.94
60°-sector	DM	Half-wavelength dipoles	7	2π	7.98	7.49	1.91	–
60°-sector	DM	radially-directed HVPs	7	2π	7.98	8.58	31.40	−12.25
60°-sector	DM	max-directed HVPs	7	2π	7.98	8.71	326.17	−8.56
60°-sector	DM	Binomial-weighted radially-directed HVPs	7	2π	7.98	6.64	39.97	–
120°-sector	DM	radially-directed HVPs	21	6π	15.14	15.19	37.22	3.53
120°-sector	DM	Binomial-weighted radially-directed HVPs	21	6π	15.14	11.21	47.83	−25.00
120°-sector	DM	max-directed HVPs	21	6π	15.14	15.22	337.18	4.93
120°-sector	DM	Binomial-weighted max-directed HVPs	21	6π	15.14	11.33	327.91	−18.19
Full	DM	Unconstrained RQ half-wavelength dipoles	13	2π	10.99	12.92	7.40	–
Full	DM	Constrained RQ half-wavelength dipoles	13	2π	10.99	12.04	100.00	3.76
Semi-circular	DM	Unconstrained RQ half-wavelength dipoles	7	2π	10.99	10.26	7.81	–
Semi-circular	DM	Constrained RQ half-wavelength dipoles	7	2π	10.99	6.62	100.00	2.08
60°-sector	DM	Unconstrained RQ half-wavelength dipoles	7	2π	7.98	9.92	12.95	4.23
60°-sector	DM	Constrained RQ half-wavelength dipoles	7	2π	7.98	9.69	100.00	4.36
Semi-circular	DM	Unconstrained RQ max-directed HVPs	7	2π	10.99	12.38	325.60	3.70
60°-sector	DM	Unconstrained RQ max-directed HVPs	7	2π	7.98	11.70	334.24	4.42

and 60°-sector RQ-unconstrained max-directed HVP arrays are superior to those of the corresponding half-wavelength versions. In fact, the semi-circular half-wavelength one is not even superdirective. The HVP-based arrays naturally produced higher FTBR values. Similarly, their maximum directivities are also higher as a consequence of their unidirectional advantage. Nevertheless, are there other optimization approaches which actually take advantage of the circular nature of the UCA directly to achieve yet better performance?

VI. Acoustic Array Eigenbeam Decomposition and Synthesis Approach

Receiving circular arrays are simple configurations whose OMs do not have left-right ambiguities. Consequently, they are convenient and advantageous as arrays of sensors. Moreover, if their DMs have high directivity values, they can provide directed beams over the entire range of 360° azimuthal directions. Both modes are useful, e.g., for DOA applications.

The use of eigenbeams have been an exceptionally successful approach to the realization of superdirective acoustic receiving arrays [45], [71]–[78]. The eigenbeam decomposition and synthesis (EBDS) method was introduced in a series of papers [77], [78] in the context of receiving arrays with ideal isotropic radiators in a spherically isotropic noise field. The optimal solution is decomposed into multipole sub-solutions which facilitate combinations of them that lead to higher-order superdirective results.

A UCA with an even number of elements, N, is assumed for this approach. The angle positions of the N elements remain as $\phi_n = n\Delta_\phi$, where $n = 0, 1, \ldots, N-1$ and $\Delta_\phi = 2\pi/N$. Examples below take ϕ_0 to be along the x-axis. The column vector of the steering phases relative to the element locations is

$$\overrightarrow{SV}(\theta,\phi) = [v_0(\theta,\phi), v_1(\theta,\phi), \ldots, v_{N-1}(\theta,\phi)]^{\mathrm{T}} \qquad (27)$$

where T denotes the transpose and its n-th component is the now familiar directive phase term:

$$v_n(\theta,\phi) = \mathrm{e}^{\mathrm{j}ka\sin\theta\cos(\phi-\phi_n)} \qquad (28)$$

Consider the column vector

$$\vec{M}_n = \frac{1}{N^{1/2}}\,[\,1, \mathrm{e}^{\mathrm{j}(n\Delta_\phi)}, \mathrm{e}^{\mathrm{j}2(n\Delta_\phi)}, \ldots, \mathrm{e}^{\mathrm{j}(N-1)(n\Delta_\phi)}]^{\mathrm{T}} \qquad (29)$$

Each component of $\vec{M}_n$ represents different powers of the phase corresponding to the n-th element of the array: $\mathrm{e}^{\mathrm{j}n\Delta_\phi}$. Forming a circulant matrix with the outer product of the $\vec{M}_m$,

$$\overline{\overline{\mathrm{CM}}} = \sum_{n=0}^{N-1} \mathrm{ev}_n \left(\vec{M}_n^* \otimes \vec{M}_n^T \right) \qquad (30)$$

one finds that the $\vec{M}_n$ are its eigenvectors and their corresponding eigenvalues are the ev_n. Its inverse is simply

$$\overline{\overline{\mathrm{CM}}}^{-1} = \sum_{n=0}^{N-1} \frac{1}{\mathrm{ev}_n} \left(\vec{M}_n^* \otimes \vec{M}_n^T \right) \qquad (31)$$

For isotropic elements in a spherically isotropic noise field, the eigenvalues are:

$$\mathrm{ev}_n = \sum_{m=0}^{N-1} \frac{\sin\{ka\,[2\sin(|n-m|\Delta_\phi/2)]\}}{ka\,[2\sin(|n-m|\Delta_\phi/2)]} e^{\mathrm{j}m(n\Delta_\phi)} \qquad (32)$$

where the linear distance between elements n and m is $a\,[2\sin(|n-m|\Delta_\phi/2)$. The eigenvalue is essentially the sum of the integrals of the difference in the phase between one element and all of the others. Because the matrix $\overline{\overline{\mathrm{CM}}}$ is symmetric and real-valued, the eigenvectors satisfy $\vec{M}_m = \vec{M}_{N-m}^*$. Similarly the eigenvalues are real and satisfy $\mathrm{ev}_m = \mathrm{ev}_{N-m}^*$, where $m = 1, 2, \ldots, N-2$. These properties can save significant compute times when N is very large.

If $\vec{w}(\theta_0,\phi_0)$ is the column vector of excitation weights to achieve the DM with its maximum directivity in the specified direction (θ_0,ϕ_0), the desired DM's beam pattern is simply the inner product

$$DM_{\mathrm{BP,max}}(\theta,\phi) = \vec{w}^{\mathrm{H}}(\theta_0,\phi_0) \cdot \overrightarrow{SV}(\theta,\phi) \qquad (33)$$

where H indicates the Hermitian transpose. Since the directivity is readily written as the Rayleigh quotient:

$$D = \frac{\left| \vec{w}^{\mathrm{H}} \cdot \overrightarrow{SV} \right|^2}{\vec{w}^{\mathrm{H}} \cdot \overline{\overline{\mathrm{CM}}} \cdot \vec{w}} \qquad (34)$$

the associated RQ-optimization procedure yields these optimal weights as

$$\vec{w}(\theta_0,\phi_0) = \overline{\overline{\mathrm{CM}}}^{-1} \cdot \overrightarrow{SV}(\theta_0,\phi_0) \qquad (35)$$

The maximum directivity is then

$$D_{\mathrm{max}} = \overrightarrow{SV}(\theta_0,\phi_0)^{\mathrm{H}} \cdot \overline{\overline{\mathrm{CM}}}^{-1} \cdot \overrightarrow{SV}(\theta_0,\phi_0) \qquad (36)$$

This analysis approach allows one to represent the optimized pattern (33) as a sum of multipole-based eigenbeams, $\mathrm{EB}_n(\theta,\phi)$, as

$$\mathrm{EB}_n(\theta,\phi) = \frac{1}{N}\mathrm{Real}\left\{ \left[\sum_{p=0}^{N-1} v_p^*(\theta_0,\phi_0)\mathrm{e}^{\mathrm{j}p(n\Delta_\phi)} \right] \right.$$
$$\left. \times \left[\sum_{q=0}^{N-1} v_q(\theta,\phi)\mathrm{e}^{-\mathrm{j}q(n\Delta_\phi)} \right] \right\} \qquad (37)$$

$$DM_{\mathrm{BP,max}}(\theta,\phi) = \sum_{n=0}^{N-1} \frac{1}{\mathrm{ev}_n}\mathrm{Real}\left\{ \left[\overrightarrow{SV}^{\mathrm{H}}(\theta_0,\phi_0) \cdot \vec{M}_n \right] \right.$$
$$\left. \times \left[\vec{M}_n^{\mathrm{H}} \cdot \overrightarrow{SV}(\theta,\phi) \right] \right\}$$
$$= \sum_{n=0}^{N-1} \frac{\mathrm{EB}_n(\theta,\phi)}{\mathrm{ev}_n} \qquad (38)$$

The maximum directivity then follows as a sum of the maximum directivity of each eigenbeam:

$$D_{\max} = \sum_{n=0}^{N-1} \frac{\left| \vec{M}_n^T \cdot \vec{SV}^*(\theta_0, \phi_0) \right|^2}{ev_n} = \sum_{n=0}^{N-1} \frac{EB_n(\theta_0, \phi_0)}{ev_n} \qquad (39)$$

where, for clarity, $\max[EB_n(\theta, \phi)] = EB_n(\theta_0, \phi_0)$. Thus, $D_{\max}$ is expressed as a sum corresponding to different orders of eigenbeams. It increases as more elements are included in the array and, hence, higher order eigenbeams become accessible.

This eigenbeam approach is applied to a 12-element UCA of isotropic radiators with $ka = 0.25\pi$, i.e., the radius of the array is $a = \lambda_0/8$, which is eight times smaller than the previous $ka = 2\pi$ cases. Six eigenbeams, $n = 0, 1, \ldots, 5$, were constructed according to (37). The normalized patterns of the $n = 1$ and $n = 4$ cases are shown in Figures 15 (a) and (b), respectively. Clearly, they represent a dipole mode and a higher order azimuthal multipole mode. They are normalized by their maximum directivity, i.e., 1.58 for $n = 1$ and 1.11×10^{-5} for $n = 4$. The maximum values naturally decrease as n increases. On the other hand, while the eigenvalues ev_n also decrease as n increases, they do so more rapidly, e.g., $ev_1 = 1.09$ and $ev_4 = 4.53 \times 10^{-6}$. Thus, the contributions of the higher-order eigenbeams to the directivity itself are significant. As expected, $EB_1/ev_1 = EB_1/ev_{11}$, $EB_2/ev_2 = EB_{10}/ev_{10}, \ldots, EB_5/ev_5 = EB_7/ev_7$.

The resulting DM's directivity pattern is shown in Figures 15(c) (dB linear plot) and (d) (linear scale, polar plot). These plot choices are the best portrayals of these calculated results. The maximum directivity is $D_{\text{peak,EBDS}} = 14.46$ dB (27.92) is along the specified direction and the backlobe is 4.37 dB (2.73), yielding a FTBR = 10.09 dB. The first sidelobe level is 10.50 dB, only -3.95 dB smaller than the maximum. Nonetheless, the outcome is superdirective because $D_{\text{peak,EBDS}} > D_{\max,2D} = \pi/2 = 1.57 = 1.96$ dB, by 12.50 dB.

However, if $ka = 2\pi$, the directivity pattern deteriorates significantly. The maximum drops to 10.28 dB, the backlobe increases to 9.03 dB; the first sidelobe level is 6.74 dB; and the smallest sidelobe level is 3.41 dB. The elements are simply too far apart to achieve well-defined eigenbeams. It was found that values of ka near to 0.25π give the best results with small differences (e.g., peak case is $ka = 0.15\pi$ with a 14.50 dB maximum and a FTBR = 10.12 dB). Consequently, the EBDS optimization approach appears to be best applied to small-radius receiving UCAs.

VII. EM Array BEAM Optimization

The acoustic EBDS method actually achieved a superdirective outcome with an electrically small array, i.e., the example array of isotropic sources is completely enclosed in a sphere whose $ka = \pi/4 = 0.785 < 1$. However, the outcomes were obtained with isotropic sources which can only generate acoustic waves. No isotropic EM sources exist. Nevertheless, the eigenbeam concept associated with tak-
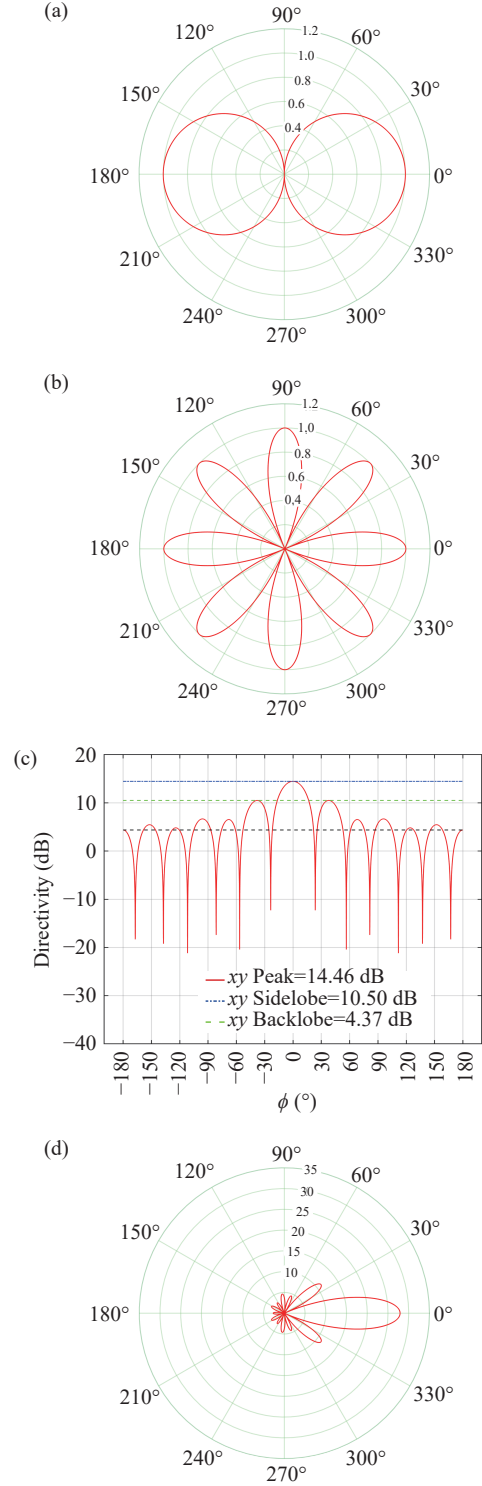

Figure 15 The EBDS results for a UCA with $ka = 0.25\pi$ that consists of 12 isotropic radiators. The specified beam direction of its DM is $(\theta_{\max}, \phi_{\max}) = (\pi/2, 0)$. (a) Eigenmode 1. (b) Eigenmode 4. (c) Directivity (dB), linear plot. (d) Directivity (linear scale), polar plot.

ing advantage of higher order multipoles to attain its superdirective results was very attractive for the potential of realizing unidirectional, high-directivity UCAs of EM elements. Consequently, the following straightforward BEAM method is developed. It is based on the azimuthal multi-

poles in the horizontal, xy-plane, and will be first applied to optimize the performance of a three-dimensional, UCA of half-wavelength vertical dipoles.

Recall that

$$\psi_m(\rho, \phi) = A_m J_m(k\rho)e^{jm\phi} \tag{40}$$

is an eigen-solution of the two-dimensional Helmholtz equation, and that one has the Bessel function identity, e.g., Eq. 11-55a in [96]:

$$e^{j\xi\cos\phi} = \sum_{m=-\infty}^{+\infty} j^m J_m(\xi)e^{jm\phi} \tag{41}$$

Therefore, the array factor of a UCA with $2N+1$ elements whose DM's main beam points in the direction (θ_0, ϕ_0) can be rewritten as a sum of eigen-solutions in the azimuthal coordinates. In particular, let the angular locations of the radiating elements in the xy-plane be specified with respect to the maximum direction in it, i.e., let $\phi_n = \phi_0 + n \times [2\pi/(2N+1)]$ for $n = -N, \ldots, 0, \ldots, N$. Then the array factor of the UCA's DM is

$$\mathcal{AF}_{\mathrm{BEAM}}(\theta, \phi) = \sum_{n=-N}^{+N} B_n e^{+jka[\sin\theta\cos(\phi-\phi_n)-\sin\theta_0\cos(\phi_0-\phi_n)]}$$

$$= \sum_{m=-\infty}^{+\infty} C_m j^m J_m(ka \sin\theta)e^{jm(\phi-\phi_0)} \tag{42}$$

where

$$C_m = \sum_{n=-N}^{+N} B_n e^{+jm(\phi_0-\phi_n)}e^{-jka \sin\theta_0\cos(\phi_0-\phi_n)} \tag{43}$$

As noted in [95], unidirectional needle radiation would be obtained if the sum of the eigen-solutions (42) was to yield

$$\delta(\phi - \phi_0) = \frac{1}{2\pi} \sum_{m=-\infty}^{+\infty} e^{jm(\phi-\phi_0)}$$

$$= \frac{1}{2\pi} + \frac{1}{\pi} \sum_{m=1}^{+\infty} \cos[m(\phi - \phi_0)] \tag{44}$$

However, we need to solve for the excitation amplitudes B_n for $n = -N, -N+1, \ldots, N$, i.e., there is not an infinite number of them, rather there are a limited number. The system of equations (42) and (43) is over-determined, a mismatch existing between the two sums needed to achieve a unique solution. Thus, the sum of the eigen-solutions will be restricted to $2N+1$ terms, i.e., the sum over the higher order azimuthal modes in (42) is restricted as

$$\mathcal{AF}_{\mathrm{BEAM}}(\theta, \phi) \approx \sum_{m=-N}^{+N} C_m j^m J_m(ka \sin\theta)e^{jm(\phi-\phi_0)} \tag{45}$$

Then the goal becomes determining the excitation coefficients that will achieve, for instance, a pseudo-needle beam outcome (other choices may be preferred depending on the application), i.e., that will realize the distribution/function:

$$\delta_N(\phi - \phi_0) = \frac{1}{2\pi} \sum_{m=-N}^{+N} e^{jm(\phi-\phi_0)} \tag{46}$$

or better.

As already demonstrated, the maximum field direction of the UCAs with the assumed z-oriented elements is broadside to them, i.e., along the xy-plane where $\theta_0 = \pi/2$. Therefore, the pseudo-needle beam would be attained, for instance, if the array factor of the DM of the UCA was to yield

$$\mathcal{AF}_{\mathrm{BEAM}}(\theta = \pi/2, \phi) = \delta_N(\phi - \phi_0) \tag{47}$$

This outcome is realized if

$$C_m = \sum_{n=-N}^{+N} B_n e^{+jm(\phi_0-\phi_n)}e^{-jka \sin\theta_0\cos(\phi_0-\phi_n)}\bigg|_{\theta_0=\pi/2}$$

$$= \frac{1}{2\pi j^m J_m(ka \sin\theta_0)}\bigg|_{\theta_0=\pi/2}$$

$$\equiv \sum_{n=-N}^{+N} B_n e^{+jm(\phi_0-\phi_n)}e^{-jka\cos(\phi_0-\phi_n)} = \frac{1}{2\pi j^m J_m(ka)} \tag{48}$$

Let the components of the matrix $\{M_{mn}\}$, where $m, n = -N, -N+1, \ldots, N$, be

$$M_{mn} = e^{+jm(\phi_0-\phi_n)}e^{-jka\cos(\phi_0-\phi_n)} \tag{49}$$

and let the vectors $\mathbf{B} = [B_N, \ldots, B_1, B_0, B_{-1}, \ldots, B_{-N}]^{\mathrm{T}}$, and $\mathbf{F} = [f_N, \ldots, f_1, f_0, f_{-1}, \ldots, f_{-N}]^{\mathrm{T}}$ with

$$f_m = \frac{1}{2\pi j^m J_m(ka)} \tag{50}$$

All of these terms can be compiled into the matrix equation: $\overline{\overline{\mathbf{M}}} \cdot \mathbf{B} = \mathbf{F}$. Since M is invertible, the excitation coefficients are then obtained immediately by matrix inversion, i.e.,

$$\mathbf{B} = \overline{\overline{\mathbf{M}}}^{-1} \cdot \mathbf{F} \tag{51}$$

Let us assume that the UCA consists of z-oriented half-wavelength dipoles. The element factor for a half-wavelength dipole is (2) with the length $L = \lambda/2$. The far-field pattern of the directional mode of such a BEAM optimized UCA is

$$\mathcal{UCA}_{\mathrm{BEAM,hw}}(\theta, \phi) = \mathcal{AF}_{\mathrm{BEAM}}(\theta, \phi) \times \mathcal{EVF}_{\mathrm{ed,hw}}(\theta, \phi) \tag{52}$$

The directivity is then obtained by calculating the intensity radiated in a specific direction and the total power radiated averaged over all space:

$$D_{\mathrm{BEAM,hw}}(\theta, \phi) = \frac{|\mathcal{UCA}_{\mathrm{BEAM,hw}}(\theta, \phi)|^2}{\frac{1}{4\pi} \int_0^{2\pi} \int_0^{\pi} |\mathcal{UCA}_{\mathrm{BEAM,hw}}(\theta, \phi)|^2 \sin\theta \, \mathrm{d}\theta \, \mathrm{d}\phi} \tag{53}$$

It has its maximum along the specified broadside direction

$(\theta_0 = \pi/2, \phi = 0)$ because $\mathcal{AF}_{\text{DM}}$ does, i.e., the directivity in the xy-plane with the desired C_m is

$$D_{\text{DM,hw}}(\theta_0, \phi) = \frac{|\mathcal{EVF}_{\text{ed,hw}}(\pi/2, \phi) \times \delta_N(\phi - \phi_0)|^2}{\frac{1}{4\pi} \int_0^{2\pi} \int_0^{\pi} |\mathcal{UCA}_{\text{DM,hw}}(\theta, \phi)|^2 \sin\theta \, d\theta \, d\phi} \tag{54}$$

The UCA of 13 z-oriented half-wavelength dipoles with $ka = 0.25\pi$, i.e., $a = \lambda_0/8$, is simulated first to illustrate its properties and to make comparisons with the other UCAs considered hitherto. The directivity results in the two vertical planes are shown in Figures 16(a) and (b). Those in the horizontal xy-plane are shown in Figures 16(c) and (d). The maximum directivity in the zx- and xy-planes is $D_{\text{max,BEAM}} = 15.00$ dB and the corresponding backlobe is -7.28 dB, which gives the FTBR = 22.28 dB. The first sidelobe level in the xy-plane is 1.91 dB, -13.09 dB below this peak value. Moreover, all sidelobe levels in the $-z$-direction are smaller than -19.75 dB below it. The maximum directivity in the yz-plane is -7.28 dB. These results are superior to those obtained already with the conventional EM approaches.

The effective width of the array is $W_{\text{eff}} = 2a = \lambda_0/4$ and its effective height is $H_{\text{eff}} = \lambda_0/2$. Therefore, its effective aperture area is $A_{\text{eff}} = W_{\text{eff}} \times H_{\text{eff}} = \lambda_0^2/8$; and, hence, the maximum directivity bound is $D_{\text{max,3D}} = 4\pi A_{\text{eff}}/\lambda_0^2 = \pi/2 = 1.96$ dB Consequently, as was the case with the acoustic EBDS method's outcomes, the BEAM results indicate that this EM array is superdirective. In fact, $D_{\text{max,BEAM}}$ is greater than $D_{\text{max,3D}}$ by 13.04 dB.

Moreover, a direct comparison of Figures 15(d) and Figure 17(a) demonstrates that the BEAM results are superior to those of the EBDS approach. These linear-scale polar plots facilitate a simpler comparison. The mainlobe is narrower. The sidelobes of its xy-plane pattern are significantly smaller. However, neither method gives exceptional results when the radius of the array is much larger, but contains only the same number of elements. It is found that when the array elements are spread too far apart angularly, the superposition of the higher order azimuthal multipoles is not as effective. For example, if the size of this 13-element half-wavelength UCA becomes $ka = 0.5\pi$, then $D_{\text{peak,BEAM}}$ decreases to 29.52 (14.70 dB). On the other hand, the directivity pattern of the corresponding 25-element UCA with $ka = 0.5\pi$ is shown in Figure 17(b). The peak directivity has increased significantly to $D_{\text{max,BEAM}} = 18.46$ dB (70.19). Even with an increased $D_{\text{max,3D}} = \pi = 4.97$ dB (3.14), the $D_{\text{max,BEAM}}$ is larger than it by 13.49 dB. Thus, this larger array is also clearly superdirective. Moreover, all sidelobe levels in the back hemisphere have become much smaller, now being -25.20 dB below this peak value.

Further investigations of the advantages of employing the max-directed HVPs over the half-wavelength dipoles was performed. It was first found that the BEAM results did not deteriorate with a smaller angular section of the circle if enough elements were present. Semi-circular arrays of 13
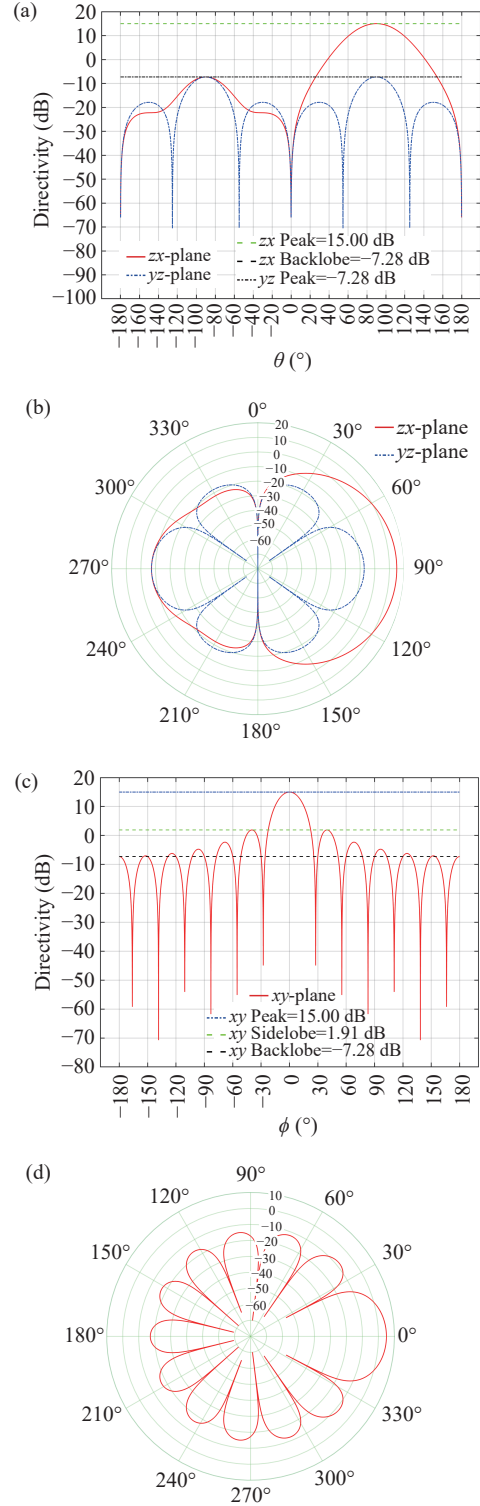

Figure 16 Directivity results for a UCA with $ka = 0.25\pi$ that consists of 13 half-wavelength dipoles and optimized with the Bessel-eigenmode approach. The specified beam direction of the DM is $(\theta_{\max}, \phi_{\max}) = (\pi/2, 0)$. (a) Vertical plane, linear plot. (b) Vertical plane, polar plot. (c) Horizontal plane, linear plot. (d) Horizontal plane, polar plot (dB).

half-wavelength dipoles and HVPs with $ka = 0.25\pi$ were simulated. The BEAM directivity results are shown in Figure 18. The horizontal plane directivity results of the half-wavelength dipole array are given in Figures 18(a)
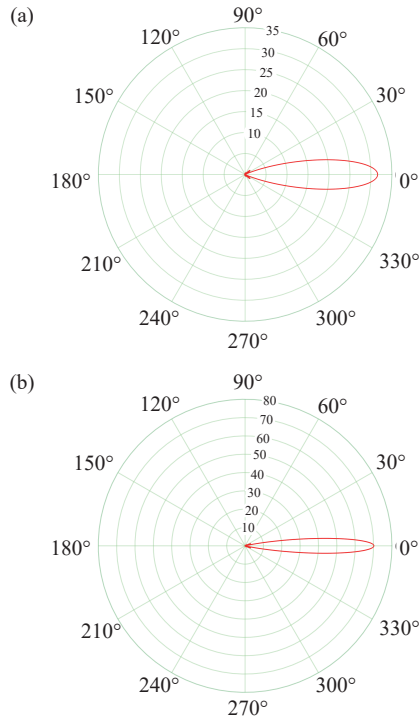
Figure 17 BEAM directivity results (polar plots in linear scale to compare with the acoustic array's) for half-wavelength UCAs of different sizes. (a) 13-element UCA with $ka = 0.25\pi$ and $D_{max,BEAM} = 31.60$ (15.00 dB). (b) 25-element UCA with $ka = 0.50\pi$ and $D_{max,BEAM} = 70.19$ (18.46 dB).

and (b). The maximum directivity, $D_{max,BEAM} = 15.00$ dB, is along the x-axis with a backlobe level of -7.28 dB, which yields the FTBR = 22.28 dB. The first sidelobe level is 1.91 dB, -13.09 dB below the maximum. The largest sidelobe level in the back hemisphere is -4.75 dB, -19.75 dB below the maximum. The yz-peak was -7.28 dB. Pleasantly, these characteristics are essentially identical to the full UCA ones. On the other hand, the corresponding max-directed HVP results of the semi-circular case of HVPs are presented in Figures 18(c) and (d). The superior performance of the max-directed HVP case are immediately observed. Details include the maximum directivity, $D_{max,BEAM}$ = 15.21 dB, being along the x-axis with a backlobe level of -331.33 dB, which yields the FTBR = 346.54 dB. Again, in addition to producing a higher maximum directivity, the max-directed HVPs produce highly desirable, exceptionally smaller fields in the back direction. While the first sidelobe level is 1.07 dB, 14.14 dB below the maximum, in the front hemisphere, the largest sidelobe level in the back hemisphere is -11.44 dB, -26.65 dB below the maximum. The yz-peak is smaller at -11.70 dB. Both arrays are clearly superdirective.

For further comparison purposes the 60°-sector array of 7 max-directed HVPs with $ka = 0.25\pi$ was also considered. The BEAM directivity results are shown in Figure 19. The patterns in the two vertical planes and the horizontal plane are given, respectively, in Figures 19(a) and (b), and in Figures 19(c) and (d). The maximum directivity,

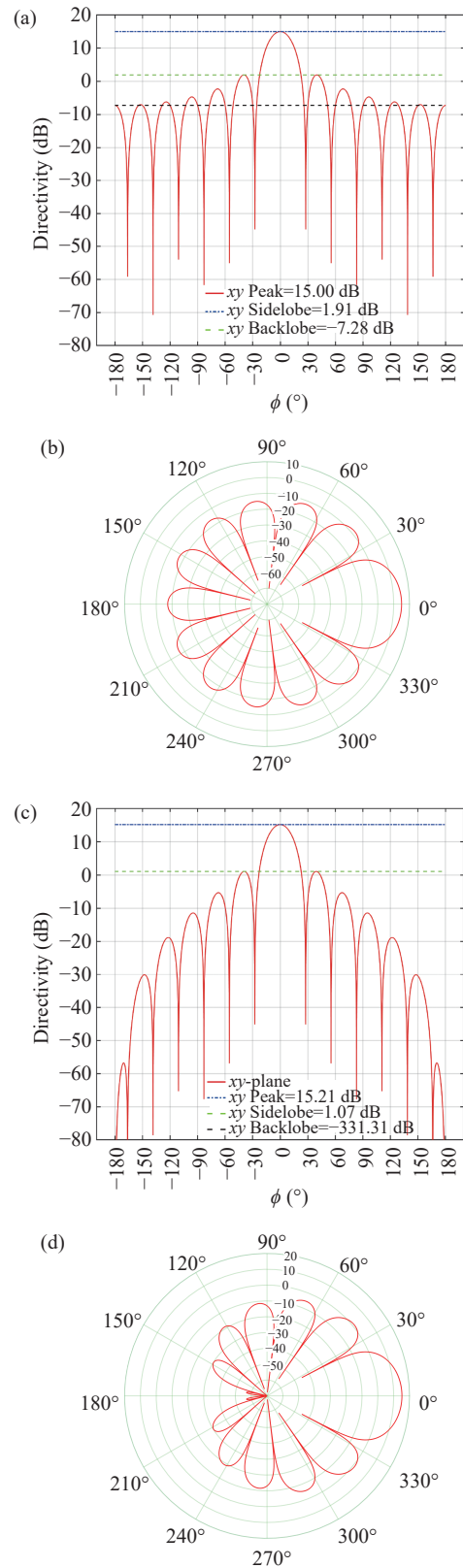**Figure 18** BEAM directivity results in the horizontal, xy-plane for 13-element semi-circular arrays with $ka = 0.25\pi$ optimized with the Bessel-eigenmode approach. The specified beam direction of the DM is $(\theta_{max}, \phi_{max}) = (\pi/2, 0)$. (a) Half-wavelength dipoles, linear plot. (b) Half-wavelength dipoles, polar plot. (c) Max-directed HVPs, linear plot. (d) Max-directed HVPs, polar plot.
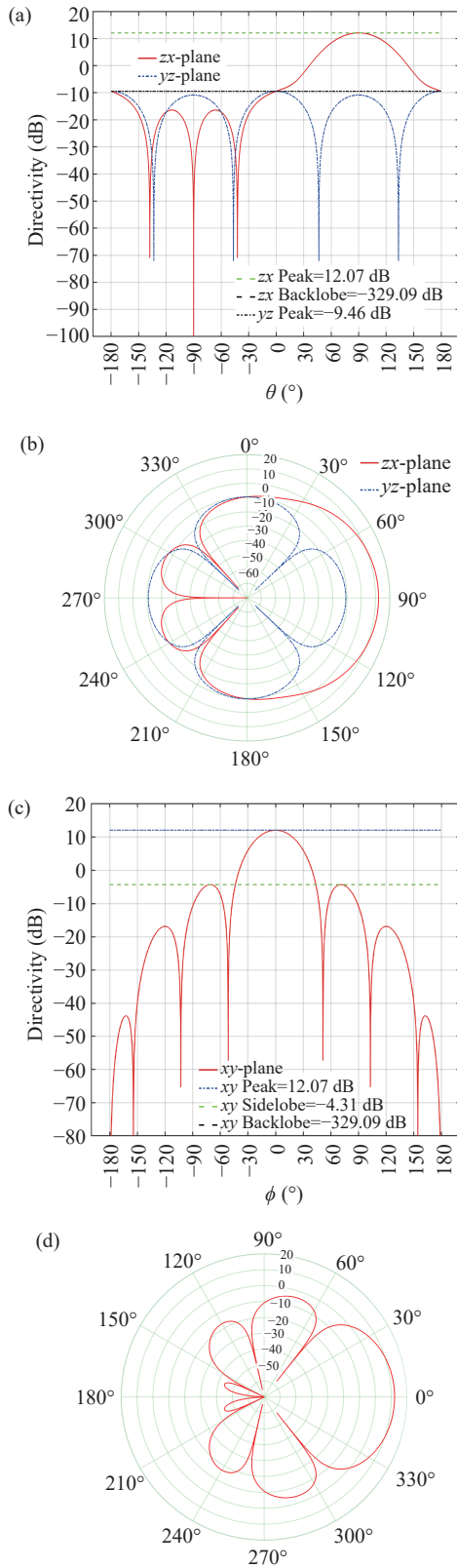
Figure 19 BEAM directivity results for the 7-element max-directed 60°-sector HVP array with $ka = 0.25\pi$ and with the specified $(\theta_{max}, \phi_{max}) = (\pi/2, 0)$. (a) Vertical planes, linear plot. (b) Vertical planes, polar plot. (c) Horizontal plane, linear plot. (d) Horizontal plane, polar plot.

$D_{max,BEAM} = 12.07$ dB, is along the x-axis with a backlobe

level of −329.09 dB, which yields the FTBR = 341.16 dB. The first sidelobe level is −4.31 dB, 16.38 dB below the maximum. The largest sidelobe level in the back hemisphere is −16.87 dB, −28.94 dB below the maximum. The yz-peak was −9.46 dB. In fact, the field levels in the back hemisphere are all below −9.46 dB, −21.53 dB below the maximum. This BEAM optimized sector case is superdirective as well. In fact, its results are superior to those of the corresponding unconstrained RQ-optimized case.

A final important comparison was made. The standard, unconstrained RQ-optimization results can be quite sensitive to the number of decimal points kept in the determined element amplitude coefficients. For the $ka = 2\pi$ semi-circular array of 13 half-wavelength dipoles optimized with the FTBR-constrained version, the maximum directivity and FTBR values were 14.92 dB and 100.00 dB keeping all 16 decimal places. Keeping only 3 of them, these values changed to 14.91 dB (very slight decrease) and 49.77 dB (large variation, but nonetheless, very acceptable unidirectional performance). Basically, this larger array was quite insensitive to small variations in the solution coefficients. On the other hand, when $ka = 0.25\pi$, the maximum directivity and FTBR values were actually 15.37 dB and 100.00 dB keeping all 16 decimal places. However, when only 6 were kept, they deteriorated significantly to 5.77 dB and 0.57 dB. The constrained RQ-optimization results were very sensitive for this significantly smaller array. In contrast, recall that the corresponding BEAM results for the $ka = 0.25\pi$ semi-circular array of 13 max-directed HVPs were 15.21 dB and 346.54 dB. These values were obtained when all 16 decimal places were kept. When only 3 were retained, these values did not change. The BEAM results were found to be highly tolerant to those not so small changes in the specified amplitude coefficients.

It must be re-emphasized that the pseudo-needle outcome was a choice and that other patterns may be more desirable for specific applications. As the process was delineated, it would be straightforward to adapt the BEAM optimization approach to achieve whatever arrangement of the far fields one desired by taking advantage of the best mixture of multipoles.

VIII. Practical Issues

As briefly noted in the introduction, the EM community has had a long history of treating superdirectivity theoretically, but then immediately dismissing it from practical points of view. This consensus opinion was nicely summarized in 1989 by R.W.P. King in [52] at the beginning of Section II where he emphasizes: "The supergain theorem states that it is theoretically possible to design an antenna with arbitrarily small dimensions and a directivity as high as desired. It follows from a proof by Oseen [43] that the theorem is consistent with Maxwell's equations. The general consensus has been that superdirective antennas are impractical because of critical tolerances, narrow bandwidth, and very low efficiency [97], [98]." This statement echoed an earlier

one of the same nature in [99]. However, I believe that there was a true inflection point in the history of and attitudes towards superdirective arrays in the mid-2000's with the already noted set of papers by Dr. Arthur Yaghjian and his Hanscom AFB colleagues in which they experimentally demonstrated superdirective, electrically small, two-element end-fire arrays. The additional references provided in the introduction simply highlight the reality that there have been many articles describing successfully tested superdirective end-fire (linear) arrays since then, effectively over the last two decades. In fact, these issues have become quite popular recently, e.g., with recent reports of more end-fire [100]–[104] and even broadside-radiating [105], [106] systems. These EM community successes follow better theoretical understandings of the phenomena, enhanced numerical simulators, and the associated earnest explorations into novel feeding concepts, lower-loss materials, and unconventional radiator designs that are overcoming the traditional stigma attached to the anticipated practical drawbacks.

Given the many noted successes associated with acoustic UCAs, the superdirective outcomes of the various approaches used to custom-design the EM UCA exemplars studied herein will hopefully stimulate the necessary fabrication and testing of their pathfinder concepts to guide further evolution of their subsequent prototypes into practical systems. Our very preliminary practical considerations to experimentally verify these concepts has begun by taking immediate advantage of the acumen developed from the EM UCA challenges experienced in [107]. As suggested earlier, the eventual aims would be to replace the vertical dipoles of such a UCA with the corresponding adaptations of the electrically small, highly efficient, coplanar twin-line differential-fed HVPs reported in [80], [87]. Initial design studies with numerical simulations of a UCA of radially-pointing versions of those HVPs have been performed. They account for all of the mutual coupling and impedance matching effects and have already yielded promising results. We hope to report on these independent efforts in the future.

IX. Conclusions

The performance characteristics of several full, semi-circular, and sector UCAs of electric dipoles and HVP elements were considered. Different optimization techniques were applied to maximize their directivity and FTBR values. The intent was to determine which techniques and arrays achieved superdirective performance. It was confirmed that an odd-number of elements in a full UCA produce OMs with superior OoR results. The unconstrained (constrained) RQ-approach applied to the full half-wavelength dipole array achieved a DM with superdirective (and unidirectional) properties. The semi-circular arrays of HVPs, with no optimization and with the unconstrained-RQ optimization, were superdirective with significant, natural unidirectional properties. The two multipole-based approaches – the acoustic EBDS method and the innovative BEAM approach devel-

oped herein – applied to significantly smaller-radius arrays also achieved superdirective outcomes. The BEAM technique produced superior directivity and FTBR results.

Comparisons between the arrays of dipole and HVP elements clearly demonstrated that the unidirectional Huygens elements produced superior performance characteristics. For large radius arrays, the unconstrained and constrained RQ-optimization methods produced superdirective properties that were quite tolerant to changes in the amplitude coefficients they specified. It was not the case for small radius ones. On the other hand, both the EBDS and BEAM approaches produced very good results for the small radius arrays, but did not for the large, sparsely populated ones. The BEAM results for those small radius, hence, densely-populated arrays were shown to be quite tolerant to changes in the excitation amplitudes the method prescribed.

While only one ring of elements was treated in this study, several rings could be optimized to produce further enhanced and practical performance characteristics. As shown in [5], this outcome was true even for the DMs of both sector and full multi-ring UCAs of electric monopoles. Furthermore, a system with several circular ring arrays, each at different heights along the z-axis could provide multiple beam coverage of the azimuth from the ensuing multiple sector-DMs, each having superdirective properties. This multi-beam capability, which is in demand for 5G and NextG wireless systems, could also be facilitated with more effort in a single ring by taking into account and adjusting for the superposition of the fields in any overlapping regions of those beams. In either case, the appropriate feed-networks and associated electronics that would deliver the requisite amplitudes and phases to each element would have to be developed. Given the reported practical successes of superdirective acoustic receiving arrays designed with the EBDS approach, it is expected that the presented BEAM analysis and simulation results for several types of EM UCAs will lead to practical transmitting or receiving versions that have the superdirective, unidirectional performances reported herein.

Appendix A

The conversions of Spherical-coordinate unit vectors to Cartesian unit vectors are

$$\hat{r} = \sin\theta\cos\phi\,\hat{x} + \sin\theta\sin\phi\,\hat{y} + \cos\theta\,\hat{z}$$
$$\hat{\theta} = \cos\theta\cos\phi\,\hat{x} + \cos\theta\sin\phi\,\hat{y} - \sin\theta\,\hat{z}$$
$$\hat{\phi} = -\sin\phi\,\hat{x} + \cos\phi\,\hat{y} \tag{A-1}$$

The conversions of Cartesian unit vectors to spherical-coordinate unit vectors are

$$\hat{x} = \sin\theta\cos\phi\,\hat{r} + \cos\theta\cos\phi\,\hat{\theta} - \sin\phi\,\hat{\phi}$$
$$\hat{y} = \sin\theta\sin\phi\,\hat{r} + \cos\theta\sin\phi\,\hat{\theta} + \cos\phi\,\hat{\phi}$$
$$\hat{z} = \cos\theta\,\hat{r} - \sin\theta\,\hat{\theta} \tag{A-2}$$

Cyclic permutation of the spherical-coordinate unit vectors yields

$$\hat{r} = \hat{\theta} \times \hat{\phi}$$
$$\hat{\phi} = \hat{r} \times \hat{\theta}$$
$$\hat{\theta} = \hat{\phi} \times \hat{r} \qquad (\text{A-3})$$

Cyclic permutation of the Cartesian unit vectors yields

$$\hat{z} = \hat{x} \times \hat{y}$$
$$\hat{y} = \hat{z} \times \hat{x}$$
$$\hat{x} = \hat{y} \times \hat{z} \qquad (\text{A-4})$$

Cross-products used to define electric and magnetic dipole fields (spherical-coordinate unit vectors):

$$\hat{r} \times \hat{r} \times \hat{z} = \sin\theta \, \hat{\theta}$$
$$\hat{r} \times \hat{z} = -\sin\theta \, \hat{\phi}$$
$$\hat{r} \times \hat{r} \times \hat{x} = -\cos\theta \cos\phi \, \hat{\theta} + \sin\phi \, \hat{\phi}$$
$$\hat{r} \times \hat{x} = \sin\theta \, \hat{\theta} + \cos\theta \cos\phi \, \hat{\phi}$$
$$\hat{r} \times \hat{r} \times \hat{y} = -\cos\theta \sin\phi \, \hat{\theta} - \cos\phi \, \hat{\phi}$$
$$\hat{r} \times \hat{y} = -\cos\phi \, \hat{\theta} + \cos\theta \sin\phi \, \hat{\phi} \qquad (\text{A-5})$$

Cross-products used to define electric and magnetic dipole fields (Cartesian-coordinate unit vectors):

$$\hat{r} \times \hat{x} = \cos\theta \, \hat{y} - \sin\theta \sin\phi \, \hat{z}$$
$$\hat{r} \times \hat{r} \times \hat{x} = (-\sin^2\theta \sin^2\phi - \cos^2\theta) \, \hat{x}$$
$$+ \sin^2\theta \sin\phi \cos\phi \, \hat{y} + \sin\theta \cos\theta \cos\phi \, \hat{z} \qquad (\text{A-6})$$

$$\hat{r} \times \hat{y} = -\cos\theta \, \hat{x} + \sin\theta \cos\phi \, \hat{z}$$
$$\hat{r} \times \hat{r} \times \hat{y} = \sin^2\theta \sin\phi \cos\phi \, \hat{x}$$
$$+ (-\cos^2\theta - \sin^2\theta \cos^2\phi) \, \hat{y} + \sin\theta \cos\theta \sin\phi \, \hat{z} \qquad (\text{A-7})$$

$$\hat{r} \times \hat{z} = \sin\theta \sin\phi \, \hat{x} - \sin\theta \cos\phi \, \hat{y}$$
$$\hat{r} \times \hat{r} \times \hat{z} = \sin\theta \cos\theta \cos\phi \, \hat{x} + \sin\theta \cos\theta \sin\phi \, \hat{y} - \sin^2\theta \, \hat{z} \qquad (\text{A-8})$$

Then, for example,

$$\vec{\mathcal{P}}(\theta, \phi) = \hat{r} \times \hat{r} \times \hat{z} + \hat{r} \times (\sin\phi_n \, \hat{x} - \cos\phi_n \, \hat{y})$$
$$= [\sin\theta \cos\theta \cos\phi \, \hat{x} + \sin\theta \cos\theta \sin\phi \, \hat{y} - \sin^2\theta \, \hat{z}]$$
$$+ \sin\phi_n[\cos\theta \, \hat{y} - \sin\theta \sin\phi \, \hat{z}]$$
$$- \cos\phi_n[-\cos\theta \, \hat{x} + \sin\theta \cos\phi \, \hat{z}]$$
$$= [\sin\theta \cos\theta \cos\phi - \cos\theta \cos\phi_n] \, \hat{x}$$
$$+ [\sin\theta \cos\theta \sin\phi + \cos\theta \sin\phi_n] \, \hat{y}$$
$$+ [-\sin^2\theta - \sin\theta(\sin\phi \sin\phi_n + \cos\phi \cos\phi_n)] \, \hat{z}$$
$$= \cos\theta[\sin\theta \cos\phi - \cos\phi_n] \, \hat{x}$$
$$+ \cos\theta[\sin\theta \sin\phi - \sin\phi_n] \, \hat{y}$$
$$- \sin\theta[\sin\theta + \cos(\phi - \phi_n)] \, \hat{z} \qquad (\text{A-9})$$

which immediately yields

$$\vec{\mathcal{P}}(\theta = \pi/2, \phi) = -[1 + \cos(\phi - \phi_n)] \, \hat{z} \qquad (\text{A-10})$$

References

[1] W. W. Hansen and J. R. Woodyard, "A new principle in directional antenna design," *Proceedings of the Institute of Radio Engineers*, vol. 26, no. 3, pp. 333–345, 1938.

[2] W. W. Hansen and L. M. Hollingsworth, "Design of "flat-shooting" antenna arrays," *Proceedings of the IRE*, vol. 27, no. 2, pp. 137–143, 1939.

[3] H. L. Knudsen, "The necessary number of elements in a directional ring aerial," *Journal of Applied Physics*, vol. 22, no. 11, pp. 1299–1306, 1951.

[4] Y. Liu, H. Liu, and S. X. Gong, "A wideband horizontally polarized omnidirectional antenna using tightly coupled array mechanism," in *Proceedings of 2017 International Workshop on Antenna Technology: Small Antennas, Innovative Structures, and Applications*, Athens, Greece, pp. 135–136, 2017.

[5] Y. B. Wen, P. Y. Qin, G. M. Wei, *et al*., "Circular array of endfire Yagi-Uda monopoles with a full 360° azimuthal beam scanning," *IEEE Transactions on Antennas and Propagation*, vol. 70, no. 7, pp. 6042–6047, 2022.

[6] P. C. Chen, Y. Zhao, X. J. Yang, *et al*., "High-gain omnidirectional transmitarray antenna," *IEEE Transactions on Antennas and Propagation*, vol. 71, no. 11, pp. 8441–8449, 2023.

[7] P. Ioannides and C. A. Balanis, "Uniform circular and rectangular arrays for adaptive beamforming applications," *IEEE Antennas and Wireless Propagation Letters*, vol. 4, pp. 351–354, 2005.

[8] P. Ioannides and C. A. Balanis, "Uniform circular arrays for smart antennas," *IEEE Antennas and Propagation Magazine*, vol. 47, no. 4, pp. 192–206, 2005.

[9] G. Fikioris, R. W. P. King, and T. T. Wu, "The resonant circular array of electrically short elements," *Journal of Applied Physics*, vol. 68, no. 2, pp. 431–439, 1990.

[10] G. Fikioris, R. W. P. King, and T. T. Wu, "Novel surface-wave antenna," *IEE Proceedings - Microwaves, Antennas and Propagation*, vol. 143, no. 1, pp. 1–6, 1996.

[11] D. Margetis, G. Fikioris, J. M. Myers, *et al*., "Highly directive current distributions: General theory," *Physical Review E*, vol. 58, no. 2, pp. 2531–2547, 1998.

[12] O. Christogeorgos, A. Papathanasopoulos, P. J. Papakanellos, *et al*., "Benchmarking computational electromagnetics with the large resonant circular array of electrically short and thick dipoles," *IEEE Transactions on Antennas and Propagation*, vol. 71, no. 3, pp. 2661–2673, 2023.

[13] R. F. Harrington, "Reactively controlled directive arrays," *IEEE Transactions on Antennas and Propagation*, vol. 26, no. 3, pp. 390–395, 1978.

[14] K. Gyoda and T. Ohira, "Design of electronically steerable passive array radiator (ESPAR) antennas," in *Proceedings of IEEE Antennas and Propagation Society International Symposium. Transmitting Waves of Progress to the Next Millennium. 2000 Digest. Held in Conjunction with: USNC/URSI National Radio Science Meeting*, Salt Lake City, UT, USA, vol. 2, pp. 922–925, 2000.

[15] D. V. Thiel and S. Smith, *Switched Parasitic Antennas for Cellular Communications*. Artech House, Norwood, MA, USA, 2001.

[16] R. Schlub, J. W. Lu, and T. Ohira, "Seven-element ground skirt monopole ESPAR antenna design from a genetic algorithm and the finite element method," *IEEE Transactions on Antennas and Propagation*, vol. 51, no. 11, pp. 3033–3039, 2003.

[17] R. Schlub and D. V. Thiel, "Switched parasitic antenna on a finite ground plane with conductive sleeve," *IEEE Transactions on Antennas and Propagation*, vol. 52, no. 5, pp. 1343–1347, 2004.

[18] H. Kawakami and T. Ohira, "Electrically steerable passive array radiator (ESPAR) antennas," *IEEE Antennas and Propagation Magazine*, vol. 47, no. 2, pp. 43–50, 2005.

[19] M. Taromaru and T. Ohira, "Electronically steerable parasitic array radiator antenna – Principle, control theory and its applications," in *Proceedings of International Union of Radio Science General Assembly*, New Delhi, India, 2005.

[20] Q. Luo, S. Gao, X. X. Yang, *et al*., "Low-cost beam-reconfigurable directional antennas for advanced communications," in *Antenna and Array Technologies for Future Wireless Ecosystems*, Y.

J. Guo and R. W. Ziolkowski, Eds. John Wiley & Sons, Inc., Hoboken, NJ, USA, pp. 83–117, 2022.

[21] T. Liang, Y. S. Pan, and Y. D. Dong, "Miniaturized pattern-Reconfigurable multimode antennas with continuous beam-steering capability," *IEEE Transactions on Antennas and Propagation*, vol. 71, no. 6, pp. 4704–4713, 2023.

[22] E. Taillefer, A. Hirata, and T. Ohira, "Direction-of-arrival estimation using radiation power pattern with an ESPAR antenna," *IEEE Transactions on Antennas and Propagation*, vol. 53, no. 2, pp. 678–684, 2005.

[23] M. Burtowy, M. Rzymowski, and L. Kulas, "Low-profile ESPAR antenna for RSS-based DoA estimation in IoT applications," *IEEE Access*, vol. 7, pp. 17403–17411, 2019.

[24] M. Groth, M. Rzymowski, K. Nyka, *et al*., "ESPAR antenna-based WSN node with DoA estimation capability," *IEEE Access*, vol. 8, pp. 91435–91447, 2020.

[25] A. Golovkov, A. Zhuravlev, and P. Terenteva, "Omnidirectional in the azimuth plane antennas based on circular arrays with horizontal polarization for radio monitoring systems," in *Proceedings of the 2020 9th Mediterranean Conference on Embedded Computing*, Budva, Montenegro, pp. 1–4, 2020.

[26] G. R. Friedrichs, M. A. Elmansouri, and D. S. Filipovic, "A machine learning enhanced small circular array for amplitude only direction finding," in *Proceedings of 2021 IEEE International Symposium on Antennas and Propagation and USNC-URSI Radio Science Meeting*, Singapore, pp. 1479–1480, 2021.

[27] L. Marantis, D. Rongas, A. Paraskevopoulos, *et al*., "Pattern reconfigurable ESPAR antenna for vehicle-to-vehicle communications," *IET Microwaves, Antennas & Propagation*, vol. 12, no. 3, pp. 280–286, 2018.

[28] C. Devitt and J. Venkataraman, "Beam steering circular arrays in elevation and azimuth planes for automotive radar applications," in *Proceedings of 2021 IEEE International Symposium on Antennas and Propagation and USNC-URSI Radio Science Meeting*, Singapore, pp. 995–996, 2021.

[29] V. Singh, M. Khalily, and R. Tafazolli, "A metasurface-based electronically steerable compact antenna system with reconfigurable artificial magnetic conductor reflector elements," *Iscience*, vol. 25, no. 12, article no. 105549, 2022.

[30] C. W. Lin and A. Grbic, "Field synthesis with azimuthally varying, cascaded, cylindrical metasurfaces using a wave matrix approach," *IEEE Transactions on Antennas and Propagation*, vol. 71, no. 1, pp. 796–808, 2023.

[31] M. Barbuto, M. Longhi, A. Monti, *et al*., "Smart antennas 2.0," in *Proceedings of the 2023 17th European Conference on Antennas and Propagation*, Florence, Italy, pp. 1–3, 2023.

[32] S. Vellucci, M. Longhi, A. Monti, *et al*., "Phase-gradient Huygens' metasurface coatings for dynamic beamforming in linear antennas," *IEEE Transactions on Antennas and Propagation*, vol. 71, no. 10, pp. 7752–7765, 2023.

[33] M. Longhi, S. Vellucci, M. Barbuto, *et al*., "Array synthesis of circular Huygens metasurfaces for antenna beam-shaping," *IEEE Antennas and Wireless Propagation Letters*, vol. 22, no. 11, pp. 2649–2653, 2023.

[34] I. Alexeff, T. Anderson, S. Parameswaran, *et al*., "Experimental and theoretical results with plasma antennas," *IEEE Transactions on Plasma Science*, vol. 34, no. 2, pp. 166–172, 2006.

[35] T. Anderson, "Theory, measurements, and prototypes of plasma antennas," in *Proceedings of 2014 IEEE Antennas and Propagation Society International Symposium*, Memphis, TN, USA, pp. 567–568, 2014.

[36] H. Ja'afar, M. T. B. Ali, A. N. B. Dagang, *et al*., "A reconfigurable monopole antenna with fluorescent tubes using plasma windowing concepts for 4.9-GHz application," *IEEE Transactions on Plasma Science*, vol. 43, no. 3, pp. 815–820, 2015.

[37] T. Anderson, D. Melazzi, and V. Lancellotti, "An overview of experimental and numerical results on the performance of plasma antennas arrays," in *Proceedings of the 2015 9th European Conference on Antennas and Propagation*, Lisbon, Portugal, pp. 1–4, 2015.

[38] F. S. M. Armaki and S. A. M. Armaki, "Design and fabrication of plasma Yagi–Uda array antenna with beamforming," *IEEE Transactions on Plasma Science*, vol. 47, no. 5, pp. 2567–2570, 2019.

[39] T. Anderson, *Plasma Antennas*, 2nd ed., Artech House, Norwood, MA, USA, 2020.

[40] C. Wang, W. X. Shi, B. Yuan, *et al*., "Pattern-steerable endfire plasma array antenna," *IEEE Transactions on Antennas and Propagation*, vol. 69, no. 10, pp. 6994–6998, 2021.

[41] X. Ye, Y. G. Wang, J. F. Yao, *et al*., "Radiation pattern in a tunable plasma window antenna," *Journal of Physics D: Applied Physics*, vol. 55, no. 34, article no. 345201, 2022.

[42] M. Jha, N. Panghal, R. Kumar, *et al*., "Reconfigurable plasma antenna array for beamsteering application at S-band," in *Proceedings of 2022 IEEE Microwaves, Antennas, and Propagation Conference*, Bangalore, India, pp. 1403–1406, 2022.

[43] C. W. Oseen, "Die einsteinsche nadelstichstrahlung und die Maxwellschen gleichungen," *Annalen der Physik*, vol. 374, no. 19, pp. 202–204, 1922.

[44] M. T. Ivrlač and J. A. Nossek, "High-efficiency super-gain antenna arrays," in *Proceedings of 2010 URSI International Symposium on Electromagnetic Theory*, Berlin, Germany, pp. 859–860, 2010.

[45] M. Crocco and A. Trucco, "Design of robust superdirective arrays with a tunable tradeoff between directivity and frequency-invariance," *IEEE Transactions on Signal Processing*, vol. 59, no. 5, pp. 2169–2181, 2011.

[46] M. Gustafsson and S. Nordebo, "Optimal antenna currents for Q, superdirectivity, and radiation patterns using convex optimization," *IEEE Transactions on Antennas and Propagation*, vol. 61, no. 3, pp. 1109–1118, 2013.

[47] J. Diao and K. F. Warnick, "Poynting streamlines, effective area shape, and the design of superdirective antennas," *IEEE Transactions on Antennas and Propagation*, vol. 65, no. 2, pp. 861–866, 2017.

[48] H. Jaafar, S. Collardey, and A. Sharaiha, "Characteristic modes approach to design compact superdirective array with enhanced bandwidth," *IEEE Transactions on Antennas and Propagation*, vol. 66, no. 12, pp. 6986–6996, 2018.

[49] S. Mikki, S. Clauzier, and Y. Antar, "A correlation theory of antenna directivity with applications to superdirective arrays," *IEEE Antennas and Wireless Propagation Letters*, vol. 18, no. 5, pp. 811–815, 2019.

[50] Y. Karasawa, "Maximum gain of array antenna with closely placed dipole elements," *IEEE Antennas and Wireless Propagation Letters*, vol. 21, no. 8, pp. 1674–1677, 2022.

[51] K. Dovelos, S. D. Assimonis, H. Q. Ngo, *et al*., "Superdirective arrays with finite-length dipoles: Modeling and new perspectives," in *Proceedings of 2022 IEEE Global Communications Conference*, Rio de Janeiro, Brazil, pp. 6517–6522, 2022.

[52] R. W. P. King, "Supergain antennas and the Yagi and circular arrays," *IEEE Transactions on Antennas and Propagation*, vol. 37, no. 2, pp. 178–186, 1989.

[53] E. E. Altshuler, T. H. O'Donnell, A. D. Yaghjian, *et al*., "A monopole superdirective array," *IEEE Transactions on Antennas and Propagation*, vol. 53, no. 8, pp. 2653–2661, 2005.

[54] T. H. O'Donnell and A. D. Yaghjian, "Electrically small superdirective arrays using parasitic elements," in *Proceedings of 2006 IEEE Antennas and Propagation Society International Symposium*, Albuquerque, NM, USA, pp. 3111–3114, 2006.

[55] A. D. Yaghjian, T. H. O'Donnell, E. E. Altshuler, *et al*., "Electrically small supergain end-fire arrays," *Radio Science*, vol. 43, no. 3, pp. 1–13, 2008.

[56] S. R. Best, E. E. Altshuler, A. D. Yaghjian, *et al*., "An impedance-matched 2-element superdirective array," *IEEE Antennas and Wireless Propagation Letters*, vol. 7, pp. 302–305, 2008.

[57] A. D. Yaghjian, "Increasing the supergain of electrically small antennas using metamaterials," in *Proceedings of the 2009 3rd Euro-*

pean Conference on Antennas and Propagation, Berlin, Germany, pp. 858–860, 2009.

[58] M. Pigeon, C. Delaveaud, L. Rudant, *et al*., "Miniature directive antennas," *International Journal of Microwave and Wireless Technologies*, vol. 6, no. 1, pp. 45–50, 2014.

[59] A. Clemente, M. Pigeon, L. Rudant, *et al*., "Design of a super directive four-element compact antenna array using spherical wave expansion," *IEEE Transactions on Antennas and Propagation*, vol. 63, no. 11, pp. 4715–4722, 2015.

[60] A. Clemente, C. Jouanlanne, and C. Delaveaud, "Analysis and design of a four-element superdirective compact dipole antenna array," in *Proceedings of the 2017 11th European Conference on Antennas and Propagation*, Paris, France, pp. 2700–2704, 2017.

[61] A. Debard, A. Clemente, C. Delaveaud, *et al*., "Limitations and optimization of supergain end-fire arrays," in *Proceedings of the 2019 13th European Conference on Antennas and Propagation*, Krakow, Poland, pp. 1–4, 2019.

[62] A. Debard, A. Clemente, A. Tornese, *et al*., "On the maximum end-fire directivity of compact antenna arrays based on electrical dipoles and Huygens sources," *IEEE Transactions on Antennas and Propagation*, vol. 71, no. 1, pp. 299–308, 2023.

[63] K. Buell, H. Mosallaei, and K. Sarabandi, "Metamaterial insulator enabled superdirective array," *IEEE Transactions on Antennas and Propagation*, vol. 55, no. 4, pp. 1074–1085, 2007.

[64] T. Kokkinos and A. P. Feresidis, "Electrically small superdirective endfire arrays of metamaterial-inspired low-profile monopoles," *IEEE Antennas and Wireless Propagation Letters*, vol. 11, pp. 568–571, 2012.

[65] A. Haskou, A. Sharaiha, and S. Collardey, "Design of small parasitic loaded superdirective end-fire antenna arrays," *IEEE Transactions on Antennas and Propagation*, vol. 63, no. 12, pp. 5456–5464, 2015.

[66] O. S. Kim, S. Pivnenko, and O. Breinbjerg, "Superdirective magnetic dipole array as a first-order probe for spherical near-field antenna measurements," *IEEE Transactions on Antennas and Propagation*, vol. 60, no. 10, pp. 4670–4676, 2012.

[67] R. W. Ziolkowski, "Using huygens multipole arrays to realize unidirectional needle-like radiation," *Physical Review X*, vol. 7, no. 3, article no. 031017, 2017.

[68] R. W. Ziolkowski, "Mixtures of multipoles — Should they be in your EM toolbox?" *IEEE Open Journal of Antennas and Propagation*, vol. 3, pp. 154–188, 2022.

[69] T. Shi, M. C. Tang, R. L. Chai, *et al*., "Multipole-based electrically small unidirectional antenna with exceptionally high realized gain," *IEEE Transactions on Antennas and Propagation*, vol. 70, no. 7, pp. 5288–5301, 2022.

[70] R. W. Ziolkowski, "Superdirective unidirectional mixed-multipole antennas: Designs, analysis, and simulations," *IEEE Transactions on Antennas and Propagation*, vol. 71, no. 7, pp. 5566–5581, 2023.

[71] H. Cox, R. Zeskind, and T. Kooij, "Practical supergain," *IEEE Transactions on Acoustics, Speech, and Signal Processing*, vol. 34, no. 3, pp. 393–398, 1986.

[72] C. P. Mathews and M. D. Zoltowski, "Eigenstructure techniques for 2-D angle estimation with uniform circular arrays," *IEEE Transactions on Signal Processing*, vol. 42, no. 9, pp. 2395–2407, 1994.

[73] H. Teutsch and W. Kellermann, "Acoustic source detection and localization based on wavefield decomposition using circular microphone arrays," *The Journal of the Acoustical Society of America*, vol. 120, no. 5, pp. 2724–2736, 2006.

[74] Y. Wang, Y. X. Yang, Y. L. Ma, *et al*., "High-order superdirectivity of circular sensor arrays mounted on baffles," *Acta Acustica united with Acustica*, vol. 102, no. 1, pp. 80–93, 2016.

[75] Y. Wang, Y. X. Yang, and Y. L. Ma, "Arbitrary-order superdirectivity of circular sensor arrays," *The Journal of the Acoustical Society of America*, vol. 148, no. 3, pp. 1425–1435, 2020.

[76] Y. Wang, X. Y. Li, L. Yang, *et al*., "Robust superdirective beamforming for arbitrary sensor arrays," *Applied Acoustics*, vol. 210, article no. 109462, 2023.

[77] Y. L. Ma, Y. X. Yang, Z. Y. He, *et al*., "Theoretical and practical solutions for high-order superdirectivity of circular sensor arrays," *IEEE Transactions on Industrial Electronics*, vol. 60, no. 1, pp. 203–209, 2013.

[78] Y. Wang, Y. X. Yang, Y. L. Ma, *et al*., "Robust high-order superdirectivity of circular sensor arrays," *The Journal of the Acoustical Society of America*, vol. 136, no. 4, pp. 1712–1724, 2014.

[79] R. W. Ziolkowski, "Electrically small antenna advances for current 5G and evolving 6G and beyond wireless systems," in *Antenna and Array Technologies for Future Wireless Ecosystems*, Y. J. Guo and R. W. Ziolkowski, Eds. Wiley-IEEE Press, Hoboken, NJ, USA, pp. 335–391, 2022.

[80] W. Lin and R. W. Ziolkowski, "Theoretical analysis of beam-steerable, broadside-radiating Huygens dipole antenna arrays and experimental verification of an ultrathin prototype for wirelessly powered IoT applications," *IEEE Open Journal of Antennas and Propagation*, vol. 2, pp. 954–967, 2021.

[81] C. A. Balanis, *Antenna Theory: Analysis and Design*, 4th ed., John Wiley & Sons, Hoboken, NJ, USA, 2016.

[82] P. Jin and R. W. Ziolkowski, "Metamaterial-inspired, electrically small Huygens sources," *IEEE Antennas and Wireless Propagation Letters*, vol. 9, pp. 501–505, 2010.

[83] R. W. Ziolkowski, "Low profile, broadside radiating, electrically small Huygens source antennas," *IEEE Access*, vol. 3, pp. 2644–2651, 2015.

[84] M. C. Tang, H. Wang, and R. W. Ziolkowski, "Design and testing of simple, electrically small, low-profile, Huygens source antennas with broadside radiation performance," *IEEE Transactions on Antennas and Propagation*, vol. 64, no. 11, pp. 4607–4617, 2016.

[85] W. Lin and R. W. Ziolkowski, "Electrically small, low-profile, Huygens circularly polarized antenna," *IEEE Transactions on Antennas and Propagation*, vol. 66, no. 2, pp. 636–643, 2018.

[86] R. W. Ziolkowski, "AWE-inspiring electrically small antennas," *Reviews of Electromagnetics*, vol. 1, no. 1, pp. 1–29, 2021.

[87] W. Lin and R. W. Ziolkowski, "Electrically small, single-substrate Huygens dipole rectenna for ultracompact wireless power transfer applications," *IEEE Transactions on Antennas and Propagation*, vol. 69, no. 2, pp. 1130–1134, 2021.

[88] S. J. Orfanidis, *Electromagnetic Waves and Antennas*, Rutgers University, Piscataway, NJ, USA, 2002.

[89] R. Harrington, "Antenna excitation for maximum gain," *IEEE Transactions on Antennas and Propagation*, vol. 13, no. 6, pp. 896–903, 1965.

[90] D. Cheng and F. Tseng, "Gain optimization for arbitrary antenna arrays," *IEEE Transactions on Antennas and Propagation*, vol. 13, no. 6, pp. 973–974, 1965.

[91] F. I. Tseng and D. Cheng, "Gain optimization for arbitrary antenna arrays subject to random fluctuations," *IEEE Transactions on Antennas and Propagation*, vol. 15, no. 3, pp. 356–366, 1967.

[92] L. Jelinek and M. Capek, "Optimal currents on arbitrarily shaped surfaces," *IEEE Transactions on Antennas and Propagation*, vol. 65, no. 1, pp. 329–341, 2017.

[93] M. Gustafsson, M. Capek, and K. Schab, "Tradeoff between antenna efficiency and Q-factor," *IEEE Transactions on Antennas and Propagation*, vol. 67, no. 4, pp. 2482–2493, 2019.

[94] M. Gustafsson and M. Capek, "Maximum gain, effective area, and directivity," *IEEE Transactions on Antennas and Propagation*, vol. 67, no. 8, pp. 5282–5293, 2019.

[95] S. Arslanagić and R. W. Ziolkowski, "Highly subwavelength, superdirective cylindrical nanoantenna," *Physical Review Letters*, vol. 120, no. 23, article no. 237401, 2018.

[96] C. A. Balanis, *Advanced Engineering Electromagnetics*, 2nd ed., Wiley, Hoboken, NJ, USA, 2012.

[97] L. J. Chu, "Physical limitations of omni-directional antennas," *Journal of Applied Physics*, vol. 19, no. 12, pp. 1163–1175, 1948.

[98] T. T. Taylor, "A discussion of the maximum directivity of an antenna," *Proceedings of the IRE*, vol. 36, no. 9, article no. 1135, 1948.

[99] R. C. Hansen, "Fundamental limitations in antennas," *Proceedings of the IEEE*, vol. 69, no. 2, pp. 170–182, 1981.

[100] A. Tornese, A. Clemente, and C. Delaveaud, "Loaded and loadless supergain parasitic end-fire arrays," in *Proceedings of the 2024 18th European Conference on Antennas and Propagation*, Glasgow, UK, pp. 1–5, 2024.

[101] A. Touhami, S. Collardey, and A. Sharaiha, "Challenges and limits of designing wideband and efficient compact superdirective antenna," in *Proceedings of the 2024 18th European Conference on Antennas and Propagation*, Glasgow, UK, pp. 1–4, 2024.

[102] D. P. Lynch, V. Fusco, M. M. Tentzeris, *et al.*, "Super-realized gain Huygens antennas," in *Proceedings of the 2024 18th European Conference on Antennas and Propagation*, Glasgow, UK, pp. 1–3, 2024.

[103] J. Moore, A. M. Graham, M. M. Tentzeris, *et al.*, "Low-profile super-realised gain antennas," in *Proceedings of the 2024 18th European Conference on Antennas and Propagation*, Glasgow, UK, pp. 1–4, 2024.

[104] I. Kanbaz, O. Yurduseven, and M. Matthaiou, "Optimization of super-directive linear arrays with differential evolution for high realized gain," in *Proceedings of the 2024 18th European Conference on Antennas and Propagation*, Glasgow, UK, pp. 1–5, 2024.

[105] R. W. Ziolkowsk, "Self-resonant broadside-radiating superdirective unidirectional mixed-multipole antennas," in *Proceedings of 2024 18th European Conference on Antennas and Propagation*, Glasgow, UK, pp. 1–5, 2024.

[106] R. W. Ziolkowsk, "Superdirective broadside-radiating unidirectional mixed-multipole antenna arrays," in *Proceedings of the 2024 18th European Conference on Antennas and Propagation*, Glasgow, UK, pp. 1–5, 2024.

[107] G. M. Wei, Y. L. Wang, Y. He, *et al.*, "Ultra-wideband vertically polarized long-slot circular phased array," *IEEE Transactions on Antennas and Propagation*, vol. 72, no. 5, pp. 4161–4172, 2024.

Richard W. Ziolkowski received (magna cum laude) the B.S. degree (Hons.) in physics from Brown University, Providence, RI, USA, in 1974; the M.S. and Ph.D. degrees in physics from the University of Illinois at Urbana-Champaign, Urbana, IL, USA, in 1975 and 1980, respectively; and an Honorary Doctorate degree from the Technical University of Denmark, Kongens Lyngby, Denmark in 2012.

He is currently a Professor Emeritus with the Department of Electrical and Computer Engineering at the University of Arizona, Tucson, AZ, USA. He was a Litton Industries John M. Leonis Distinguished Professor in the College of Engineering as well as a Professor in the College of Optical Sciences until his retirement in 2018. He was also a Distinguished Professor in the Global Big Data Technologies Centre in the Faculty of Engineering and Information Technologies (FEIT) at the University of Technology Sydney, Ultimo NSW Australia from 2016 until 2023. He was the Computational Electronics and Electromagnetics Thrust Area Leader with the Engineering Research Division of the Lawrence Livermore National Laboratory before joining The University of Arizona in 1990.

Prof. Ziolkowski was the recipient of the 2019 IEEE Electromagnetics Award (IEEE Technical Field Award). He is an IEEE Life Fellow as well as a Fellow of OPTICA (previously the Optical Society of America, OSA) and the American Physical Society (APS). He was the 2014–2015 Fulbright Distinguished Chair in Advanced Science and Technology (sponsored by DSTO, the Australian Defence Science and Technology Organisation). He served as the President of the IEEE Antennas and Propagation Society (AP-S) in 2005 and has had many other AP-S leadership roles. He is also actively involved with the International Union of Radio Science (URSI) and the European Association on Antennas and Propagation (EurAAP). He is the co-editor of the best-selling 2006 IEEE-Wiley book, *Metamaterials: Physics and Engineering Explorations*, and an author and co-editor of the recent Wiley-IEEE Press books: *Advanced Antenna Array Engineering for 6G and Beyond Wireless Communications* (2022) and *Antenna and Array Technologies for Future Wireless Ecosystems* (2022), respectively. (Email: ziolkows@arizona.edu)